

Whipping instability characterization of an electrified visco-capillary jet

GUILLAUME RIBOUX¹†, ÁLVARO G. MARÍN¹,
IGNACIO G. LOSCERTALES² AND ANTONIO BARRERO¹

¹Escuela Técnica Superior de Ingenieros, Departamento de Ingeniería Aeroespacial y Mecánica de Fluidos, Universidad de Sevilla, Av. de los Descubrimientos s/n, 41092, Sevilla, Spain

²Escuela Técnica Superior de Ingenieros Industriales, Universidad de Málaga, C/Pedro Ortiz Ramos, s/n 29071, Málaga, Spain

(Received 23 March 2010; revised 4 August 2010; accepted 18 October 2010;
first published online 7 February 2011)

The charged liquid micro-jet issued from a Taylor cone may develop a special type of non-axisymmetric instability, usually referred to in the literature as a *whipping* mode. This instability usually manifests itself as a series of fast and violent lashes of the charged jet, which makes its characterization in the laboratory difficult. Recently, we have found that this instability may also develop when the host medium surrounding the Taylor cone and the jet is a dielectric liquid instead of air. When the oscillations of the jet occur inside a dielectric liquid, their frequency and amplitude are much lower than those of the oscillations taking place in air. Taking advantage of this fact, we have performed a detailed experimental characterization of the whipping instability of a charged micro-jet within a dielectric liquid by recording the jet motion with a high-speed camera. Appropriate image processing yields the frequency and wavelength, among the other important characteristics, of the jet whipping as a function of the governing parameters of the experimental set-up (flow rate and applied electric field) and liquid properties. Alternatively, the results can be also written as a function of three dimensionless numbers: the capillary and electrical Bond numbers and the ratio between an electrical relaxation and residence time.

Key words: jets, microfluidics, nonlinear instability

1. Introduction

Micro-structures and nano-structures of interest in several technological fields can be generated from electro-capillary liquid jets. Among the techniques capable of generating these jets, electro-spray (Zeleny 1917; Cloupeau & Prunet-Foch 1989), coaxial electro-spray (Loscertales *et al.* 2002; López-Herrera *et al.* 2003), electro-spinning (Doshi & Reneker 1995) and coaxial electro-spinning (Loscertales *et al.* 2002; Sun *et al.* 2003) are the most popular for being able to generate particles in the nanometric range (Barrero & Loscertales 2007), micro-capsules/nano-capsules (Larsen *et al.* 2003) and ultra-fine fibres whose structures may be simple (Jaeger *et al.* 1998), hollow (Loscertales *et al.* 2004; Li & Xia 2004; Lallave *et al.* 2007) or composed of two or more layers of different materials (Díaz *et al.* 2006). These particles have a

† Email address for correspondence: griboux@us.es.

variety of applications in the drug industry, food additives and material engineering, among others.

In electro-sprays, an electrified conical meniscus (Taylor cone) is formed at the tip of a capillary tube, a thin jet issuing from the vertex cone. In the coaxial version, two or more immiscible liquids are injected through two or more concentric capillary tubes. The electrified jet emitted from the cone vertex is inherently unstable, and it undergoes instability modes due to either capillary instabilities leading to jet breakup or lateral instabilities (whipping mode) owing to the action of the electric field.

To successfully obtain nano-fibres from electrified liquid jets via electro-spinning, the capillary instability, which is responsible for the breakup of the jet into charged droplets, must be completely avoided. This occurs, for example, when the working fluid is a complex fluid such as a melt of polymers of high molecular weight dissolved in a volatile solvent. The rheological properties of these melts slow down and even prevent the growth of varicose instabilities. As is well known, large values of liquid viscosity delay the jet breakup by reducing the growth rate of axisymmetric perturbations, so longer jets may be obtained. However, non-symmetric perturbation modes can still grow because of the net charge carried by the jet. Indeed, if a small portion of the charged jet moves slightly off axis, the charge distributed along the rest of the jet will push that portion farther away from the axis, thus leading to a lateral instability known as the whipping or bending instability. The movement of the jet under this instability gives rise to very large tensile stresses, which lead to a dramatic jet thinning. The solidification process and thus the production of micro-fibres or nano-fibres increases by the rapid rise in the solvent evaporation rate due to the thinning process. For the production of nano-fibres, this technique is very competitive with the other existing ones (i.e. phase separation, self-assembly and template synthesis, among others) and is therefore the subject of intense research. These and other properties of the solutions have been termed *electro-spinnability* of a solution, i.e. the capability of a given substance of being spun into fibres by electro-spinning. Unfortunately, most of the existing literature on electro-spinning, which numbers hundreds of publications in the year 2005 alone, deals with phenomenological studies testing the electro-spinnability and properties of different polymer solutions, but only a few of them have developed theoretical models aiming to predict the behaviour of the charged jet.

The first attempt at modelling this type of instabilities dates back to Basset (1894), who calculated the growth rates of both varicose and lateral perturbations in a charged jet. Lateral, non-axial instabilities in electrified jets were reported by Zeleny (1917) at the beginning of the 20th century. Almost 60 years later, Taylor (1969) carried out the first detailed experiments on this type of jet instability and corrected the first theoretical results given by Basset. More recently, Mestel (1994, 1996) analysed the stability of an infinitely long jet in the cases of liquids with low and high viscosities.

Hohman *et al.* (2001a) developed a slender-body theory to calculate the electric field at the jet, taking into account the effects of both jet stretching and charge transport. Moreover, they carried out a linear stability analysis to obtain the growth rates of both lateral and varicose perturbations of the charged jet. They summarized their results in operating diagrams, which compared their results with those of their experimental companion paper (Hohman *et al.* 2001b). A simple analytical model for the stretching of a viscous charged jet in the presence of an electric field has been reported by Fridrikh *et al.* (2003). The model predicts that the final diameter of the jet arises from a balance between surface tension and electrostatic electrical repulsion;

the predictions quantitatively agree with electro-spun fibres produced from solutions of different polymers.

The small axisymmetric perturbations of a charged coaxial jet with two viscous liquids co-flowing in an inviscid surrounding dielectric gas under a radial electrical field have been considered in the temporal stability analysis carried out by Li, Yin & Yin (2008). Two different axisymmetric modes, i.e. the para-sinusoidal and the para-varicose mode, were found in the Rayleigh limit, the former being much more unstable than the latter. They also found that the viscosities of the two liquids and the shear at the interface have an effect on the stability of the two unstable modes. In a later work (Li, Yin & Yin 2009), these authors extended their previous study to the analysis of the non-axisymmetric modes of a charged coaxial jet. They found that the helical mode ($m = 1$) becomes dominant for high values of the liquid viscosities. Conversely, the helical mode and higher non-axisymmetric modes ($m > 1$) are stabilized by the interfacial tension. Also, sufficiently high values of the radial electric field and/or sufficiently low values of the interfacial tension favour the growth of the helical instability and result in the whipping motion of the jet. The non-symmetric perturbation of a coaxial compound non-charged jet moving in an inviscid surrounding gas has been recently considered by Ruo, Chen & Chang (2009). They found that there exist wide-range parameter domains in which the non-axisymmetric sinusoidal mode ($m = 1$) predominates. The results are summarized as a series of parametric maps which may provide qualitative guidance to either enhance or suppress the non-symmetric instability.

Reneker and co-workers (Reneker *et al.* 2000; Yarin, Koombhongse & Reneker 2001) analysed the dynamics of the electrified jet by means of a Lagrangian model. They discretized the electrified jet and studied the dynamics of each of its small segments subject to the forces acting on them: surface tension and electrical and viscoelastic forces. The model calculates rather accurately the electric field on the jet and reproduces quite successfully the shape of the whipping envelope of the jet, but it overestimates both the velocity and the displacement of the lateral movement of the jet. Its main drawback, however, lies in the difficulty of making a clear connection between the results of the model and the physical parameters that govern the phenomenon: flow rate, applied electrical field, electrical conductivity, surface tension, etc.

Recently, Barrero *et al.* (2004) operated an electro-spray in steady cone-jet mode inside a dielectric liquid medium. Although electro-sprays within a host liquid medium are ruled by the same physical principles than those operated in air, there are some differences in their behaviour mainly due to the much higher density of the liquid bath; different values of the viscosity of liquids and gases and surface tensions in liquid–liquid and liquid–gas interfaces may be also responsible for the possible differences in one or another case. The most representative example is the electro-spraying of pure glycerine; in fact, when an electro-spray of glycerine is operated in air, it gives rise to extremely long and straight jets that finally break into droplets due to capillary instabilities, while when glycerine is electro-sprayed within a hexane bath, the resulting charged jet bends some short distance downstream from the needle and develops the characteristic spiral motion of the whipping instability, as shown in figure 1(a). This different behaviour can be explained by the fact that capillary instabilities grow more slowly in liquid–liquid interfaces than in liquid–air interfaces so that lateral instabilities can develop before the breakup of the jet. Therefore, charged jets generated within dielectric liquid baths are prone to develop other instabilities different from the capillary ones.

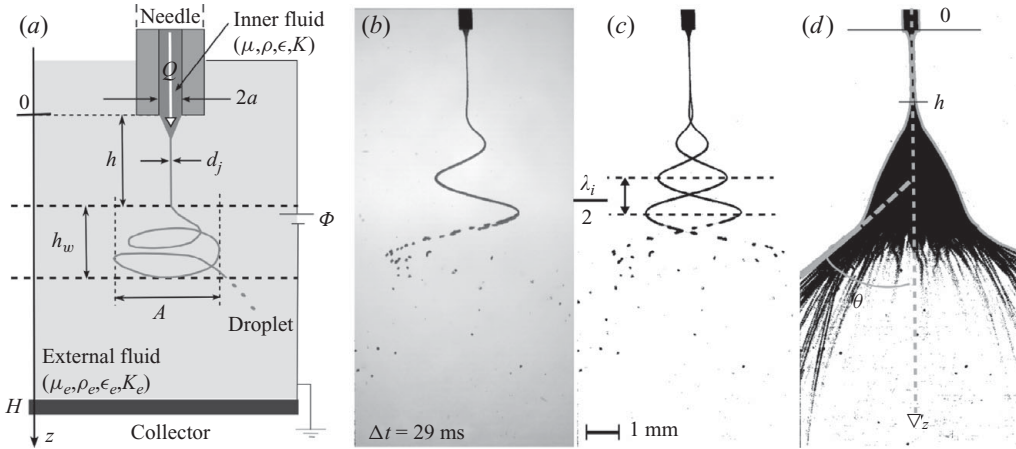


FIGURE 1. (a) Sketch of the experimental set-up. The conductive inner liquid was glycerine, while the outer one was hexane. (b) Picture showing an example of the whipping instability of the electrified jet, superimposed with a processed jet image obtained one complete period of the whipping motion later. (c) Wavelength measurements at a half-period. (d) Whipping envelope with θ the maximal angle of the droplet projection ($Q = 1.0 \text{ ml h}^{-1}$, $\Phi = 2.25 \text{ kV}$).

Another important difference is that the oscillations of the whipping instability inside a liquid are much less violent than in air; the large inertia of the liquid bath makes the frequency of the jet oscillations several orders of magnitude lower than those found in typical electro-spinning experiments (Hohman *et al.* 2001*b*; Shin *et al.* 2001; Reneker & Yarin 2008). Taking advantage of this property, we have carried out an experimental work on the whipping instability of the jet of an electro-spray of glycerine operated within a liquid (hexane) bath. We have used a set-up identical to that used in previous works on electro-sprays inside liquid media (Barrero *et al.* 2004; Marín *et al.* 2007). The main aim of the work is the characterization of the whipping instability (frequency, amplitude, wavelength) in terms of the governing parameters (flow rate, electrical field). To this end, the jet motion was recorded, and the images were digitalized and carefully processed.

The paper is organized as follows: §2 contains detailed information on the experimental set-up and the image processing. Scaling and preliminary observations are presented in §§3 and 4. Experimental results concerning the Taylor cone and straight jet are discussed in §5. The experimental characterization of the whipping mode is presented §6 before the conclusions in §7.

2. Apparatus and image processing

The experimental set-up consisted of a $38 \times 32 \text{ mm}^2$ open tank of Plexiglas with height 180 mm (see figure 1*a*). The walls of the tank were made of glass to allow visualization. The tank was filled with hexane whose viscosity, density and relative electrical permittivity were respectively $\mu_e = 0.3 \text{ mPa s}$, $\rho_e = 660 \text{ kg m}^{-3}$ and $\epsilon_e/\epsilon_o = 1.89$, where ϵ_e is the electrical permittivity of the hexane and ϵ_o is the vacuum permittivity. A round electrode collector of diameter 23 mm connected to electrical ground was located at the bottom of the tank. A metallic needle of inner radius $a = 115 \mu\text{m}$ immersed in the hexane was located at a fixed distance $H = 27 \text{ mm}$ above the collector. A conductive liquid, glycerine, was injected through the needle at a constant flow rate Q with the help of a Harvard PHD 4400

programmable syringe pump. The physical properties of the glycerine were as follows: density $\rho = 1250 \text{ kg m}^{-3}$, dynamic viscosity $\mu = 1280 \text{ mPa s}$, electrical conductivity $K = 1.7 \text{ }\mu\text{S m}^{-1}$ and electrical permittivity $\epsilon/\epsilon_o = 43$. Surface tension of the glycerine–hexane pair, $\gamma = 28.3 \text{ mN m}^{-1}$, was measured using the pendant drop method. The metallic needle was connected to a Bertan 205B-10R high-voltage power supply to impose an electric field between the collector and the needle exit. A multi-meter connected in series between the high-voltage power supply and the needle was used to measure the electrical current through the jet and to check the stability of the process. The whipping motion of the jet was captured with a Photron FASTCAM 1024 PCI high-speed video camera at an acquisition frequency of $2000 \text{ frames s}^{-1}$. A floodlight was placed facing the high-speed video camera to obtain good contrast in the jet image. The picture dimensions were 1024×512 pixels, while the resolution was within a range of $8\text{--}16 \text{ }\mu\text{m pixel}^{-1}$.

The images of the jet motion were analysed by using the image processing software ImageJ together with in-house-developed algorithms. Examples of the jet path, which appears quite neat, are presented in figure 1(*b,c*). Figure 1(*b*) shows a picture of the whipping instability with a binary image of the jet superimposed, the latter captured one complete period later. Since the picture and the binary image are almost superimposed upon each other, one may conclude that the whipping mode is periodic for the values of the governing parameters $Q = 1.0 \text{ ml h}^{-1}$ and $\Phi = 2.25 \text{ kV}$, the period of the whipping oscillations being 29 ms with an accuracy of 0.5 ms . Figure 1(*c*) shows two binary images of the jet path, separated by a semi-period (14.5 ms); the superposition of the two images permits the measurement of the wavelength λ_i of the whipping oscillation. Note that as a consequence of the electric field, the wavelength λ_i of the instability increases slightly along the z -axis. Therefore, we define a mean value λ of the wavelength by averaging the values of the measured wavelength λ_i of each jet loop along the z -axis. The envelope of the whipping jet paths can also be obtained by overlapping the jet images captured at different times. It should be noted that another possible choice for the envelope detection, such as using a video camera with long exposure time, yielded less clear results. Figure 1(*d*) shows the overlapping of 300 images of the jet and the envelope contour as a function of the distance z to the needle (grey line). Since the whipping envelope is symmetrical, an averaged meridian curve of the jet envelope is obtained as a function of the vertical distance z . We defined as h the distance between the needle exit and the point at which the whipping instability begins (figure 1*d*). The beginning of the whipping instability was defined as the jet point for which the jet envelope reaches an amplitude $A_t = 100 \text{ }\mu\text{m}$, which corresponds to $6\text{--}7$ pixels in the images. Taking different values of the threshold A_t within a range of $50\text{--}200 \text{ }\mu\text{m}$, we noted that the relative difference in the value of h was smaller than 15% . Finally, the reproducibility of the whipping motion was checked by performing six experiments at same values of the governing parameters ($Q = 0.5 \text{ ml h}^{-1}$, $\Phi = 2.0 \text{ kV}$). The results showed that the relative differences in the value of the electrical current, whipping frequency or wavelength, jet diameter and amplitude and length of the envelope were of the order of 10% , in all cases.

3. Scaling

The experimental characterization of the whipping instability of an electrified liquid jet evolving within a liquid bath is a complex problem due to the large number of physical parameters. The relevant parameters of the problem are the physical properties of the two fluids: viscosity, density, electrical permittivity, electrical

conductivity and surface tension. Also, the considered problem depends on both the geometrical parameters characterizing the experimental set-up (radius of the capillary and capillary to collector distance) and the control parameters (flow rate and the applied electrical voltage).

In the case of an electrified glycerine jet moving within a hexane bath, the number of relevant parameters is reduced because of the electrical nature and the low viscosity of the outer fluid compared with that of the glycerine. In addition, an estimate of the Reynolds number $\rho Q/(\mu a)$ based on the density, viscosity and velocity of the glycerine at the end of the needle (Higuera 2010) leads to a value of the order of 10^{-3} . Under these conditions, the inertia of the inner liquid can be neglected, and the problem can be modelled as an electrical viscous jet moving in liquid bath which in non-dimensional form is governed by six independent dimensionless parameters as follows.

Using the viscosity μ of the liquid jet, surface tension γ , capillary radius a and the electrical permittivity ϵ_e of the outer fluid as dimensional scales of the problem, we can define the following dimensionless parameters of the problem: geometrical length ratio H/a , inner-to-outer liquid electrical permittivity ratio $\beta = \epsilon/\epsilon_e$, the dimensionless number $\mathcal{S} = \rho_e \gamma a / \mu^2$ and

$$Ca = \frac{\mu Q}{\gamma a^2}, \quad \mathcal{B} = \frac{\epsilon \Phi^2}{\gamma a}, \quad \mathcal{T} = \frac{\mu K a}{\epsilon \gamma}. \quad (3.1)$$

The three last dimensionless numbers, which have already been introduced in a numerical work by Higuera (2006), respectively are as follows: the capillary number, comparing the fluid velocity Q/a^2 at the end of the capillary to the visco-capillary velocity $V_o = \gamma/\mu$; the electrical Bond number, comparing the electrical effect with the capillary effect; and a dimensionless time ratio, comparing the residence time a/V_o , the time required for a fluid particle at a velocity V_o to move across a distance a , with the electrical relaxation time ϵ/K . The residence time can also be interpreted as the time for a perturbation to propagate in the liquid (the experimental results showed that the whipping instability velocity is of the order of V_o). It is worthy of remark that defining $E_o = (\gamma/\epsilon a)^{1/2}$, $a E_o$, $\sigma_o = \epsilon E_o$ and $\epsilon E_o V_o a$ as the scales of electrical field, electrical potential, surface charge density and electrical current (Higuera 2010), in the axisymmetric case, the conservation equation of the charge in dimensionless form reads $I^* = \mathcal{T} I_b^* + I_c^*$, with

$$I_b^* = 2\pi \int_0^{r_j^*} E_z^* r^* dr^* \quad \text{and} \quad I_c^* = 2\pi r_j^* v^* \sigma^*, \quad (3.2)$$

where $[\cdot]^*$ stands for dimensionless variables; E_z^* is the axial component of the electrical field; r^* is the radial distance; r_j^* and v^* are the radius of the jet cross-section and the liquid velocity at the jet interface (Higuera 2006). The electrical field induces a conduction current I_b^* that accumulates electric charge at the surface of the jet. An additional surface current I_c^* to the conduction current is generated by the surface charge convected by the flow. Thus, the total electric current I^* is the sum of the conduction current which decreases with the distance z to the needle and the surface convection current which is null at the needle end and increases with z (Fernández de la Mora & Loscertales 1994; Gañán-Calvo, Dávila & Barrero 1997; Higuera 2010). The sum of the two electrical currents is independent of axial distance. In the conservation equation of the charge, the dimensionless parameter \mathcal{T} can be interpreted as the ratio of charge conduction transport and charge convection transport, $\mathcal{T} = I_o/I_s$, which is the ratio between an electrical conduction current scale $I_o = a^2 K E_o$ and an electrical surface convection current scale $I_s = a \sigma_o V_o$

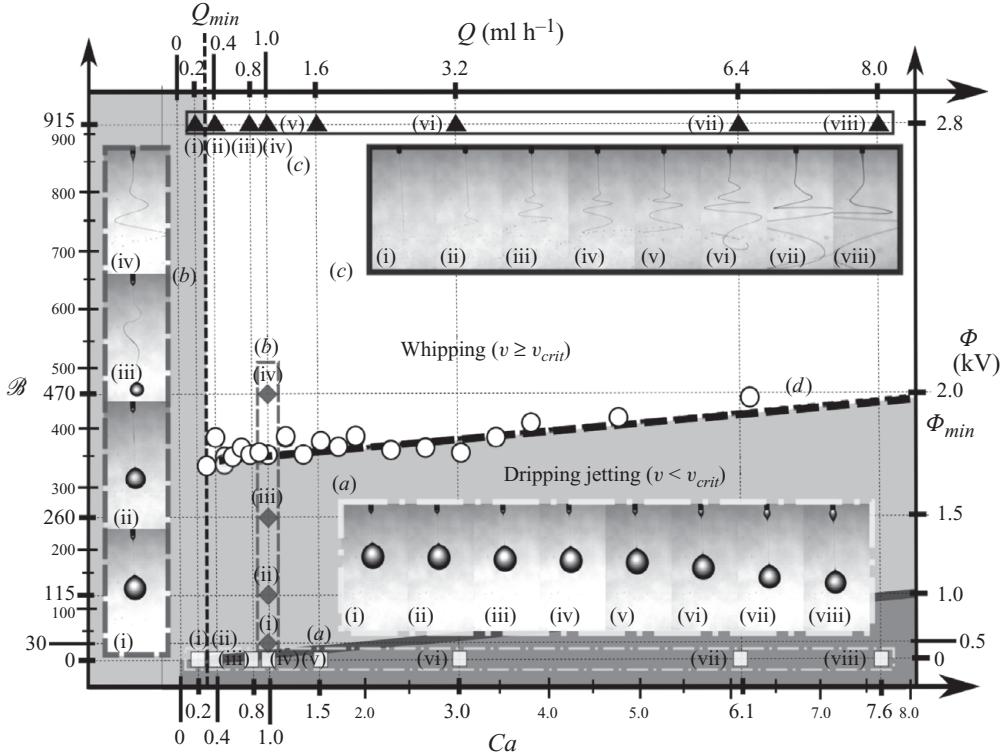


FIGURE 2. Whipping jet map for the glycerine–hexane couple ($\mathcal{T} = 19$).

that corresponds to a charge density per unit length, $a\sigma_o$, convected at the fluid velocity V_o .

The study is restricted to the experimental characterization of the whipping jet instability as a function of the supply flow rate Q and the applied electrical voltage Φ . Thus, by using the pair of fluids, glycerine–hexane, the electrical permittivity coefficient $\beta = 23$ and the dimensionless number $\mathcal{S} = 1.3 \times 10^{-3}$ were fixed. Observe that in our experiment, the dimensionless number \mathcal{S} is extremely small, indicating the relative importance of the outer flow on the jet dynamic (see the Appendix). The geometrical parameter was constant $H/a = 235$, while we varied the three dimensionless numbers within the ranges $Ca = 0.2\text{--}8.5$, $B = 300\text{--}1870$ and $\mathcal{T} = 19\text{--}27$. The variation range of the dimensionless parameter \mathcal{T} implies that the conduction electrical current in the glycerine jet is not negligible compared with the surface convection current. In contrast, the experimental conditions given in previous works on electro-sprays were such that the current transported through the jet was mostly transported by convection (Fernández de la Mora & Loscertales 1994; Gañán-Calvo *et al.* 1997); in those cases, the current varied with the flow rate, following the classical power law $I \sim Q^{1/2}$, and it was almost independent of the applied voltage, while in our case the current strongly depends on the voltage and follows a power law $I \sim Q^n$ with $n = 0.20 \pm 0.03$.

4. Preliminary observations

Figure 2 shows the *whipping map* for the fluid pair, glycerine–hexane, and yields the behaviour of the jet as a function of the control parameters Q and Φ ; it permits

identification of the region in which the jet develops an instability of the whipping type in the (Q, Φ) space or equivalently in the (Ca, \mathcal{B}) space. This type of graph was previously introduced by Hohman *et al.* (2001*b*) and Shin *et al.* (2001), who called it an *operating diagram* and considered either an electrified jet of glycerine or a jet of a mixture of polyethylene oxide (PEO) and water, evolving in air. Those diagrams are more general than ours, since, in addition to the whipping mode, they permit identification of other instability modes of the jet such as varicose, bending and steady-state jet modes.

Here, we have carried out four sets of measurements whose results are collected in figure 2.

(a) The first set of eight measurements (i–viii), represented by the square symbols, was taken at different values of the capillary number Ca (or equivalently at the corresponding values of the flow rate Q), while we kept $\mathcal{B} = \Phi = 0$. In the range of capillary numbers considered, the experimental set-up produces glycerine drops with a uniform radius of the order of 10 times the capillary radius, the frequency of the droplet formation increasing with the capillary number. A long and thin jet was formed before the complete detachment of the droplet, the length of the jet at the moment of detachment increasing linearly with the capillary number. At jet breakup, one observes the formation of a neck just behind the droplet. Lister & Stone (1998) numerically studied the capillary breakup of a viscous thread surrounded by another viscous liquid. In the case of a large internal–external viscosity ratio ($\mu/\mu_e \gg 1$), the authors reported that both the axial and radial length scales decreased linearly with the time until the jet breakup.

(b) The second set of measurements (i–iv), represented by the diamond symbols, was taken at four given values of the electrical Bond number \mathcal{B} , while the value of the capillary number was kept constant, $Ca = 1$. We observed that the diameter of the drops decreased linearly with increasing the electrical Bond number. As reported by Zhang & Basaran (1996), the length of the liquid thread before breakup also increased when the electrical Bond number increased. Furthermore, in this set of measurements, we noted clearly the transition from a dripping mode to a whipping mode, with (iii) corresponding to $\mathcal{B} = 260$ and (iv) corresponding to $\mathcal{B} = 470$. Therefore, one may define a value of the Bond number \mathcal{B}_{min} such that for $\mathcal{B} \leq \mathcal{B}_{min}$ the jet behaves in dripping mode, while it develops whipping instability when $\mathcal{B} \geq \mathcal{B}_{min}$.

(c) The third set of eight measurements (i–viii), represented by the triangular symbols, was carried out keeping the electrical Bond number at $\mathcal{B} = 915$ while varying the capillary number Ca in the range 0.2–7.6. In this case, we observed a transition from a jetting mode to a whipping mode (transition between i and ii). Thus, similar to the previous case, there exists a minimum capillary number Ca_{min} separating the jetting–whipping mode regions. Increasing the capillary number, the jet diameter and the whipping amplitude increase, and the jet motion is spatially destabilized. For $Ca = 1.5$, shown in (v), the spatial behaviour of the jet appears more chaotic than for the smaller values of Ca .

(d) Finally, we determined the transition from the dripping mode to the whipping mode in the parametric space (Ca, \mathcal{B}) by using a high-speed camera. The experimental measurements of this set, labelled as (d), are represented by the empty circles. In the range of $Ca = 0.3$ –6.2, the minimum electrical Bond number increases linearly with the capillary number. Thus, for the fluid pair, glycerine–hexane, the dripping–whipping transition boundary seems to evolve as $\mathcal{B}_{min} = 15 Ca + 340$. This equation is plotted in figure 2 as a thick dashed line. Regarding the jetting–whipping transition, we have

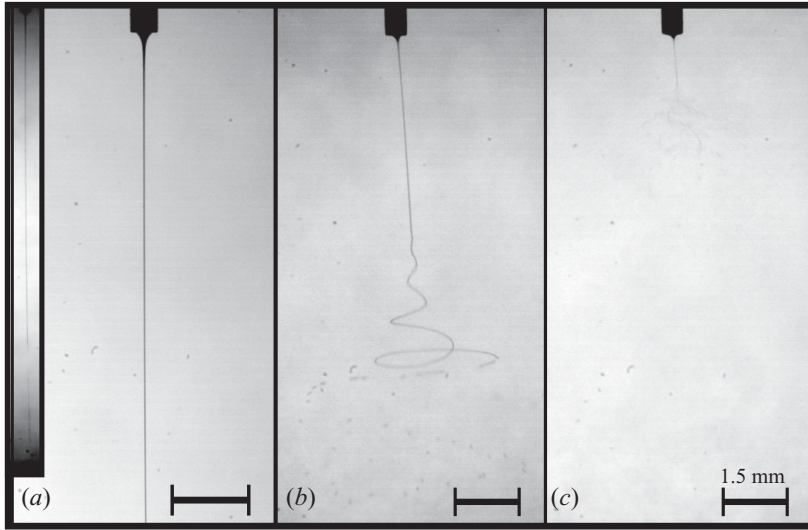


FIGURE 3. Behaviour of the electrified jet for different dimensionless time ratios \mathcal{T} ($Ca = 0.95$, $\mathcal{B} = 1860$): (a) $\mathcal{T} = 10$ (glycerine in air – the inset corresponds to a magnified view); (b) $\mathcal{T} = 23$ (glycerine $K = 1.7 \mu\text{S m}^{-1}$, in hexane); and (c) $\mathcal{T} = 190$ (glycerine $K = 14 \mu\text{S m}^{-1}$, in hexane).

found that Ca_{min} has constant value, close to 0.3, which is completely independent of the range of values of \mathcal{B} explored here.

In conclusion, the whipping instability appears only when the couple of parameters Ca and \mathcal{B} are respectively larger than Ca_{min} and \mathcal{B}_{min} . The transition from the dripping to the whipping mode occurs at a value of the electrical Bond number $\mathcal{B}_{min} = 15 Ca + 340$ within the range $0.3 \leq Ca \leq 6.2$. The transition from the jetting to the whipping mode appears at a value of the capillary number $Ca_{min} \simeq 0.3$; this value is constant and independent of the electrical Bond number \mathcal{B} . Note that the whipping mode develops within the parametric region represented by the white domain in figure 2, while no whipping instability develops into the region shown in grey.

Figure 3 shows three pictures of the glycerine jet for three different values of \mathcal{T} and the same values of both the capillary and the electrical Bond number. Figure 3(a) shows a glycerine jet in air for a value of the dimensionless time ratio $\mathcal{T} = 10$; the value of the surface tension for the glycerine–air couple is $\gamma = 64 \text{ mN m}^{-1}$. The jet motion is straight, and no instability grows within the frame of the picture. As we can observe in figure 3(a), the jet diameter does not seem to evolve along the axial (vertical) distance. This result differs from that reported in classical papers on numerical analysis of electro-sprays where the jet diameter evolved downstream as $z^{-1/4}$. The behaviour of the glycerine jet in air was observed by Hohman *et al.* (2001b), who reported that no whipping instability developed independently on the values of both the flow rate and the electrical voltage. On the other hand, in the case of a glycerine jet in a bath of hexane (figure 3b) and at the same values of the capillary and electrical Bond numbers as the previous case, the jet developed a whipping instability. The difference between the two cases is exclusively the value of the dimensionless time ratio \mathcal{T} . We have found that for \mathcal{T} smaller than a minimum value \mathcal{T}_{min} somewhere in the range between 10 and 23, the whipping instability does not develop. For a polar liquid ($\epsilon > 1$) and a dimensionless number $\mathcal{T} = 2.5$, Higuera (2006) has shown that, along the streamwise distance, the normal component of the electric field at the jet surface

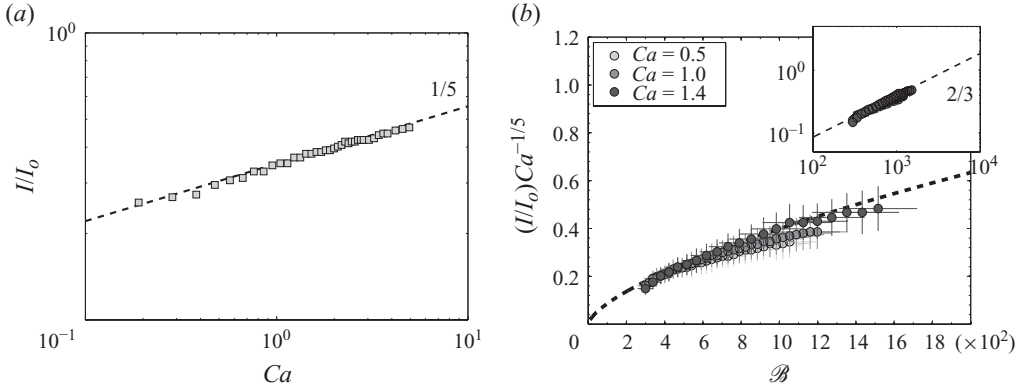


FIGURE 4. Normalized current I/I_0 as a function of (a) the capillary number Ca at $\mathcal{B} = 920$ and (b) the electrical Bond number \mathcal{B} for different Ca values ($\mathcal{T} = 23$).

is already of the order of the axial electric field. In the case of the glycerine jet in air, $\epsilon > 1$ and $\mathcal{T} = 10$, the axial electric field, comparable to the normal electrical one, works to stabilize the jet and prevent the growing of the whipping instability. When \mathcal{T} increases, the normal electric field increases too because the electrical relaxation time decreases, and the surface charge density grows towards its equilibrium value. Any arbitrary, small lateral perturbation of the jet surface may grow more easily when the axial electric field is smaller than the normal one. To confirm this hypothesis, we performed experiments with a glycerine jet in a hexane bath for two different values of the dimensionless time ratio, $\mathcal{T} = 23$ and 190 (figure 3b,c). The variation of \mathcal{T} was performed by changing the electrical conductivities of the glycerine from $K = 1.7 \mu\text{S m}^{-1}$ to $K = 14 \mu\text{S m}^{-1}$, which appear only in the definition of the time ratio. For the larger \mathcal{T} , both the whipping amplitude and the distance from the needle to the starting point of the instability are reduced, and the jet is more unstable. As expected, when the dimensionless number \mathcal{T} increases, the whipping instability grows more rapidly, and the charged jet motion is destabilized. Finally, observe that there also exists a minimum value of \mathcal{T} for which whipping instability develops. More generally, whipping instability appears only for values of Ca , \mathcal{B} and \mathcal{T} greater than the minimum ones (Ca_{\min} , \mathcal{B}_{\min} , \mathcal{T}_{\min}).

In figure 4(a), the dimensionless electrical current I/I_0 is plotted as a function of the capillary number at a given value of the electrical Bond number, $\mathcal{B} = 920$. The dimensionless current follows quite well a power law of the capillary number Ca^n with $n = 0.20 \pm 0.03$. In figure 4(b), the dimensionless current is presented as a function of the electrical Bond number for three different values of the capillary number. Provided that the dimensionless current is normalized by $Ca^{1/5}$, the three different curves collapse onto a single master curve, which follows a $2/3$ power law of the electrical Bond number. Therefore, the dimensionless electrical current I/I_0 scales as $Ca^{1/5} \mathcal{B}^{2/3}$ or equivalently as

$$I/I_0 \sim \mathcal{T} Ca^{1/5} \mathcal{B}^{2/3}, \quad (4.1)$$

where the three dimensionless parameters Ca , \mathcal{B} and \mathcal{T} appear.

When the time ratio \mathcal{T} is small enough, $\mathcal{T} < \mathcal{T}_{\min}$, the time aV_0 is of the order of the electrical relaxation time ϵ/K ; in this case, the normal electric field at the jet interface is comparable to the axial electric field. On the other hand, when $\mathcal{T} \geq \mathcal{T}_{\min}$,

the normal electric field increases because the electrical relaxation time decreases. Increasing \mathcal{T} amounts to increasing the rate of transfer of electric charge to the surface (Higuera 2006). Because the jet diameter seems not evolve as a function of the vertical distance (between the Taylor-cone apex to the distance h ; see the next section), the increase of the dimensionless number \mathcal{T} leads to an increase of charge along the jet surface. The normal electric field at the jet surface grows, and jet oscillations arise.

Expression (4.1) for the total current differs from that given by Higuera (2006). The discrepancy can be explained by the fact that the author considered small values of the electrical Bond number, $\mathcal{B} \leq 200$, which correspond to $\mathcal{B} < \mathcal{B}_{min}$, for which whipping instability does not develop for the glycerine–hexane fluid couple. Secondly, his numerical simulations were performed for a geometry of an electrode–electrode parallel plane configuration, while the experimental results presented here correspond to a capillary-electrode configuration. Note, finally, that the functional dependence of the electrical current I given here is different from that reported in the papers by Fernández de la Mora & Loscertales (1994) and Gañán-Calvo *et al.* (1997). In our case, I depends on both $Q^{1/5}$ and $\Phi^{4/3}$; the dependence of the electrical current on the applied voltage was reported by Hohman *et al.* (2001*b*), Shin *et al.* (2001) and Theron, Zussman & Yarin (2004). For electro-spinning of different polymer solutions, Theron *et al.* (2004) observed that the electrical current increases with the voltage in a nonlinear fashion, $I \sim \Phi^n$, with n in the range 2.2–4.6. Also, the authors noted an electrical current dependence on the flow rate, $I \sim Q^m$, with m between -1.04 and 0.26 . They attributed this evolution to the ion-mobility-limited charging of the solutions in their experiment. In the case of electro-spinning polymer solutions, it seems that the electrical current law as a function of the flow rate is similar to the empirical relationship observed here. In our case, the electrical current evolves more linearly as a function of the applied voltage than for the electro-spinning polymer solution.

On the contrary, Fernández de la Mora & Loscertales (1994) and Gañán-Calvo *et al.* (1997) reported the well-known $I \sim Q^{1/2}$ power law and the independence of the current on the applied voltage. As pointed out before, the main explanation for the discrepancies with our results and this law lies in the relative importance of the charge transport mechanism, conduction versus convection; in classical papers on electro-spray, the liquid properties and experimental conditions, mainly liquid conductivities and flow rates, lead to jets with very thin diameters so that convection of charge is the dominant transport mechanism, while in our case both charge conduction and convection are important.

5. Steady region: Taylor cone and straight jet

In all experimental cases presented in this section and the next, the whipping motion has been observed, since the capillary number Ca , electrical Bond number \mathcal{B} and dimensionless time ratio \mathcal{T} were larger than the minimum values (Ca_{min} , \mathcal{B}_{min} , \mathcal{T}_{min}). Therefore, all the experiments lay within the white whipping region of figure 2.

Figure 5 shows some pictures of a jet detection taken at a given instant t_i ; the whipping envelope has also been superposed upon the jet detection; it should be remembered that the whipping envelope corresponds to the maximum spatial amplitude of the lateral jet motion. In figure 5(*a–d*), the experiments were carried out at different capillary numbers and at a constant electrical Bond number, while those in figure 5(*e–h*) were performed at different electrical Bond numbers and at a fixed capillary number. For all values of both Ca and \mathcal{B} , the Taylor cone and the straight part of the jet path match very well with the whipping envelope until the beginning

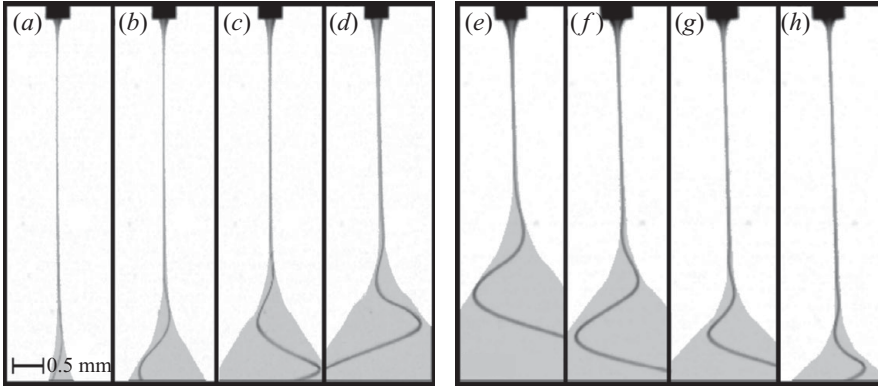


FIGURE 5. Digital jet path and whipping envelope ($\mathcal{T} = 23$): (a–d) at $\mathcal{B} = 920$, with $Ca =$ (a) 0.6, (b) 0.95, (c) 1.5 and (d) 2.5; (e–h) at $Ca = 1.0$, with $\mathcal{B} =$ (e) 645, (f) 760, (g) 980 and (h) 1160.

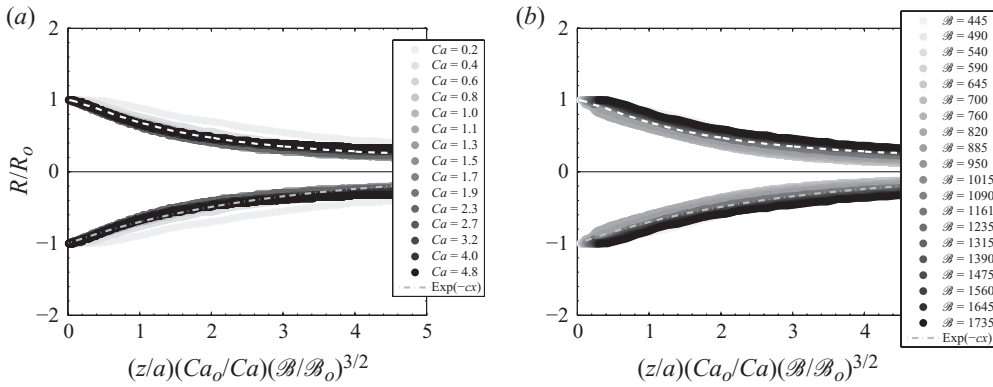


FIGURE 6. Normalized radius R of the electrified Taylor cones as a function of the dimensionless axial distance (a) for different capillary numbers at $\mathcal{B} = 920$ and (b) for different electrical Bond numbers at $Ca = 1.0$ (R_o is the radius of the cone at $z = 0$, $Ca_o = 1.0$, $\mathcal{B}_o = 645$ and $\mathcal{T} = 19$).

of the whipping instability, e.g. the distance h . The jet remains completely straight, and images of this region, taken at different times, exactly coincide when they are superposed; the jet motion is steady.

Figure 6 shows the electrified-cone radius normalized by its initial value R_o as a function of the dimensionless vertical distance z/a . The dimensionless distance was also normalized by the dimensionless expression $Ca \mathcal{B}^{-3/2}$. Figure 6(a) presents the normalized cone radius for different values of the capillary numbers at a fixed electrical Bond number, and figure 6(b) shows the influence of the electrical Bond number \mathcal{B} at fixed Ca . In figure 6(a), the mean curve of the different normalized electrified-cone radius is plotted as a dashed white line. This mean curve is also reported in figure 6(b), showing that for the range of capillary and electrical Bond numbers presented, the normalized electrified cones were self-similar when the dimensionless vertical distance z/a was normalized by the dimensionless group $Ca \mathcal{B}^{-3/2}$. One may observe that both the radial and axial length scales of the cone increase linearly with the capillary number because of the increase of the fluid velocity at the needle exit. On other

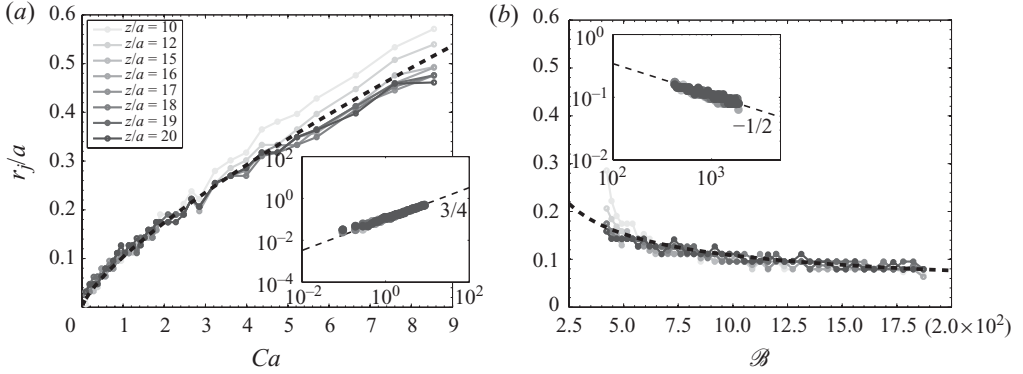


FIGURE 7. Dimensionless jet radius at different axial stations, z/a , as a function of either (a) the capillary number, with $B=920$, or (b) the electrical Bond number, with $Ca=1.0$ ($\mathcal{F}=19$).

hand, both the radius and the elongation of the electrified cones decrease as a $3/2$ power law of the electrical Bond number. The cone recedes when B increases because of the increase of the normal electrical force at the surface of the cone. Finally, in figure 6(a,b), an exponential function is plotted in a grey dashed line which shows that the electrified-cone radius decreases with the axial distance in the form

$$R/R_o = \exp[-c z/(a Ca^* B^{*-3/2})], \quad (5.1)$$

with the constant $c=0.36$, $Ca^*=Ca/Ca_o$ and $B^*=B/B_o$.

Now, we consider the influence of the dimensionless parameters on the jet radius by focusing the high-speed video camera on the steady region containing the Taylor cone and the straight part of the jet. The size of the images was 1024×512 pixels, and the error of the jet radius was estimated to be ± 1 pixel, which corresponds to $3.65 \mu\text{m}$. To estimate the effect of the capillary and electrical Bond numbers on the downstream evolution of the jet radius, measurements of r_j at different axial stations within the range $z/a=10-20$ were carried out. The two boundaries of the range were chosen to guarantee good measurements of r_j within the considered ranges of both Ca and B . For example, the minimum limit $z/a=10$ was chosen larger than the elongation of the electrified cone to ensure that the jet radius was measured instead of the electrified-cone radius.

Figure 7 shows measurements of the dimensionless jet radius r_j/a at different axial stations as a function of either the capillary number (figure 7a) or the electrical Bond number (figure 7b). The jet radius increased with the capillary number, while it decreased with the electrical Bond number. For a given pair of values of both Ca and B , observe that the jet radius remained practically constant downstream of the axial station $z/a=15$. In figure 7(a,b), a logarithmic representation of the jet radius for axial stations $z/a \geq 15$ is provided; one may conclude that the jet radius behaves downstream as

$$r_j/a = \chi Ca^{3/4} B^{-1/2}, \quad (5.2)$$

with the constant $\chi=3.29$. Expression (5.2) and the conservation of the flow rate permit the calculation of the mean liquid velocity in the jet,

$$v = V_o \frac{1}{\pi \chi^2} \left(\frac{B}{\sqrt{Ca}} \right). \quad (5.3)$$

Note that expressions (5.2) and (5.3) are valid within the range of values $0.3 \leq Ca \leq 8.5$, $420 \leq \mathcal{B} \leq 1870$ and $15 \leq z/a \leq 20$. Expression (5.3) leads to three important conclusions: in the straight part of the jet, (i) the liquid velocity accelerates when either the electrical Bond number increases or the capillary number decreases; (ii) the electrical tangential stress is negligible, since the jet velocity and jet radius are constant within the range $15 \leq z/a \leq 20$; and (iii) for an electrified jet in whipping mode and values of the dimensionless parameters Ca and \mathcal{B} such that expressions (5.2) and (5.3) are valid, the liquid velocity v in the jet is always greater than a critical velocity v_{crit} . This critical liquid velocity can be calculated using the equation $\mathcal{B} = c_1 Ca + c_2$ of the dripping–whipping transition boundary (dashed line in figure 3 with constants $c_1 = 15$ and $c_2 = 340$), which leads to

$$v_{crit} = v_{min} \left(1 + \frac{c_2}{c_1} \frac{1}{Ca} \right), \quad (5.4)$$

where $v_{min} = \zeta V_o \sqrt{Ca}$ is the first approximation to the critical velocity and $\zeta = c_1/(\pi \chi^2) = 0.44$. For the glycerine–hexane pair, the velocity $v_{min} \approx 1 \text{ cm s}^{-1}$ at $Ca = 1$. In the whipping map (figure 2), the region $v < v_{crit}$ (grey domain) corresponds to the region in which no whipping develops, while in the region $v \geq v_{crit}$ (white domain) the jet lashes. In the figure, the minimum velocity region $v < v_{min}$ and the boundary v_{min} are also shown by the dark grey domain and line.

The presence of a critical velocity governing oscillation instabilities of dynamic systems has often been observed. Typical examples are the oscillatory motion of a long ribbon hanging in an axial flow (Lemaitre, Hémon & de Langre 2005), a fluid-conveying long flexible cylinder on an elastic foundation (Doaré & de Langre 2002), a long flexible cylinder cantilevered in an outer axial flow (de Langre *et al.* 2007) and a long cylinder in the presence of an outer transverse flow. The three first cases are the result of a dynamic instability (called *flutter instability* in the literature), while the resonant coupling between the wake and the motion cylinder (*vortex induced vibrations* or VIV) accounts for the instability of the last case (Williamson & Govardhan 2004). In these examples, the structure suddenly starts to vibrate when the forcing flow velocity reaches a critical value. In the case of a visco-capillary jet subject to an electrical field at $\mathcal{T} > \mathcal{T}_{min}$, the critical velocity v_{crit} , which depends on the visco-capillary velocity V_o , seems to be the threshold value above which the whipping instability develops. Indeed, given both the capillary and electrical Bond numbers, the jet radius decreases with the axial distance up to $z \geq 15$, while beyond this station its value, given by (5.2), remains constant, and finally, the jet starts to lash at $z/a \approx 20$. In consequence, the minimum jet radius and the maximum velocity of the liquid are reached within the range $15 \leq z/a \leq 20$. Clearly, the liquid velocity must reach the velocity v expressed by (5.3) before the jet instability starts; otherwise, whipping instability does not develop. In the glycerine–hexane case, the velocity is equal to v_{crit} given by (5.4). Note that experiments using other suitable pair of liquids are necessary to determine the dependence of the coefficient ζ on the fluid properties as well as to confirm the above results.

The knowledge of the dependence of both the jet radius r_j and the electrical current I on the three dimensionless numbers Ca , \mathcal{B} and \mathcal{T} yields the electrical surface charge density $\sigma \sim I/(V_o r_j)$. In fact, using (4.1) and (5.2), we obtain, $\sigma \sim \sigma_o \mathcal{T} Ca^{-11/20} \mathcal{B}^{7/6}$, with σ_o introduced in §3; exponents in the expression of the electrical charge density were obtained experimentally, and their values are close to $-1/2$ and 1 respectively. Let us also remark that the liquid velocity v in the straight part of the jet

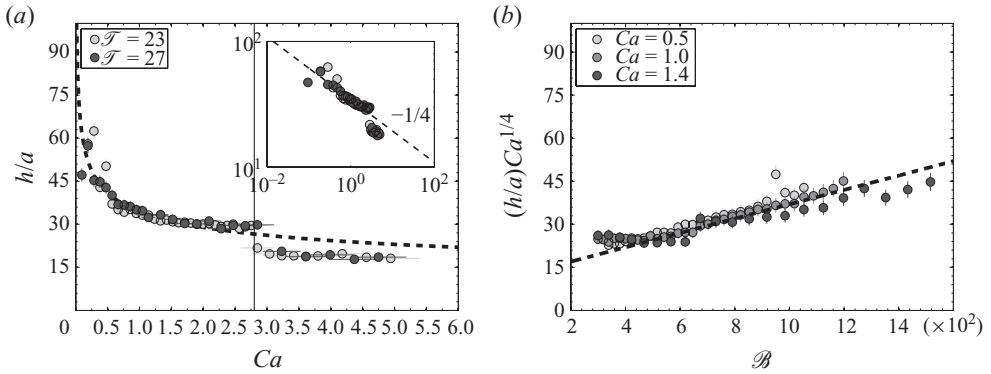


FIGURE 8. Normalized length h/a of the stable part of the jet as a function of either (a) the capillary number at two dimensionless time ratios ($\mathcal{B} = 920$) or (b) the electrical Bond number at three different capillary numbers ($\mathcal{T} = 23$).

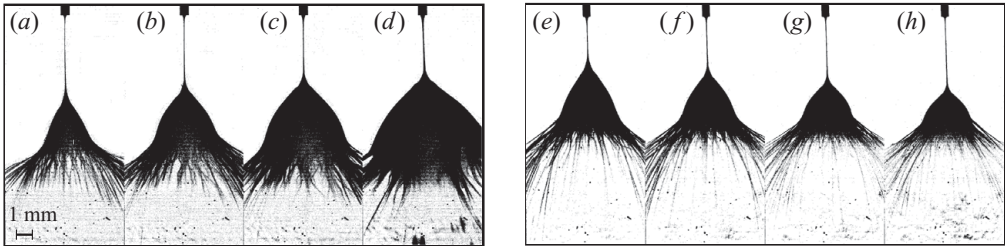


FIGURE 9. Whipping envelopes of the jet path (a–d) at constant electrical Bond number $\mathcal{B} = 920$ and four values of the capillary number $Ca =$ (a) 0.6, (b) 0.9, (c) 1.5 and (d) 2.5. In set (e–h), the capillary number was kept constant at $Ca = 1.0$, while the values of the electrical Bond number were $\mathcal{B} =$ (e) 645, (f) 760, (g) 985 and (h) 1160.

(expression (5.3)) permits a simpler relation of the surface charge density,

$$\sigma/\sigma_o \sim \mathcal{T}(v/V_o), \quad (5.5)$$

where the scaled charge density $\sigma_o \mathcal{T}$ is constant in each experiment. Thus, in the straight part of the jet, the charge density is directly proportional to the reduced velocity v/V_o corresponding to the ratio of the liquid velocity in the jet to the velocity scale of the whipping instability. In the following, it is proven that the perturbation wave velocity is proportional to V_o .

Expression (5.5) shows that σ decreases with Ca , while it increases with \mathcal{B} and \mathcal{T} . Thus, the normal electrical field also decreases (increases) with Ca (\mathcal{B}); therefore, the jet becomes more stable, and consequently, the distance h should increase when the capillary number increases or the electrical Bond number decreases. However, as shown in the following, the experimental results exhibit a behaviour that is opposite to that expected. Figure 8(a,b) show the length h of the steady part of the jet as a function of either Ca or \mathcal{B} . Awkward on purpose, h decreases with Ca (and increases with \mathcal{B}). Therefore, there must be some other instability source that needs to be taken into account to correctly explain the jet behaviour.

Figure 9 shows different pictures of the whipping envelope of the jet corresponding to a set of different experiments. The amplitude A of the envelope, which corresponds

to the maximum radial amplitude of the jet motion and to the maximum angle of the droplet trajectories with the z -axis, increases with the capillary number (see figure 9*a–d*), while it decreases with the electrical Bond number (see figure 9*e–h*). This is a consequence of the Coulomb repulsion due to the charges on the moving jet and droplets, which is much stronger in figure 9(*d*) than that in figure 9(*a*). The electric field induced by the moving charges tends to change the direction of the downstream jet trajectory. This destabilizing effect is, in this case, opposite to the stabilizing effect of decreasing the capillary number, expressed by (5.5). As shown in figure 9, the distance h decreases and the whipping of the jet begins sooner because, in the set of experiments presented here, the stabilizing effect of decreasing the capillary number is overcome by the destabilizing effect of the charged jet and droplets. Therefore, theoretical analyses of the jet behaviour exclusively based on the jet itself necessarily fail if they do not incorporate the effect of the charge downstream and in particular the charge in the whipping jet.

It should be mentioned that the shapes of the jet envelope given in figure 9 are rather similar to the shape envelope in the cases of flags flapping in wind (Zhang *et al.* 2000; Ristroph & Zhang 2008), liquid-conveying flexible pipes with a free end either in air or inside a liquid tank (Bourrières 1939) and long flexible cylinders in axial flow (Päidoussis 1998; de Langre *et al.* 2007). Bourrières (1939) reported the first study on the motion of a fluid-conveying flexible pipe with a free end; he found two different shapes of the envelope of the cylinder motion, namely a triangular form and a chalice one. Note that the shape of the envelopes shown in figure 9 are of the chalice type observed by Bourrières (1939). Also, in the case of a flapping flag under a fluid forcing (Ristroph & Zhang 2008), similar envelope shapes are observed. This similarity in the envelope shapes means that a deformable object, flexible cylinder, flag, ribbon or visco-capillary jet develops the same type of perturbation when it is subject to an appropriate excitation. In the case of both flapping flags and flexible cylinders under fluid forcing, the excitation comes from the external fluid, while in the case of a flexible pipe the excitation is due to the fluid transported through the pipe. In the case of a viscous jet into a liquid bath at rest subject to an external electrical field, the excitation comes from both the flow within the jet and the electric field (capillary and electrical Bond numbers). All these systems develop instability provided that the forcing passes a critical value; in the electrified viscous jet, whipping motion is present as long as both the capillary and electrical Bond numbers are greater than Ca_{min} and \mathcal{B}_{min} respectively or, equivalently, when the fluid velocity in the jet reaches a critical velocity v_{min} .

Figure 8(*a*) shows h/a as a function of the capillary number Ca for two values of the dimensionless time ratio and a given electrical Bond number. Note that the experimental results show that the normalized length h/a is a decreasing function, and it follows a $-1/4$ power law of the capillary number within the range $Ca = 0.1–2.8$. For $Ca \geq 2.8$, a transition in the evolution of h is observed, which strongly decreases from a value close to $30a$ down to $20a$. This transition will be explained in the next section. Measurements of h/a as a function of \mathcal{B} have been plotted in figure 8(*b*) for three different values of Ca . Provided that h/a is normalized by $Ca^{1/4}$, the three curves collapse and evolve linearly with the electrical Bond number, the slope of the h/a - \mathcal{B} curves being approximately equal to $1/40$. Thus, the length of the stable part of the jet path, h , behaves as $h \sim Ca^{-1/4} \mathcal{B}$, within the range of dimensionless parameters $Ca = 0.1–2.8$, $\mathcal{B} = 300–1515$ and $\mathcal{T} = 23–27$. Let us finally remark that h may be also related to the jet radius r_j . In effect, taking into account (5.2) and the last expression for h , one easily

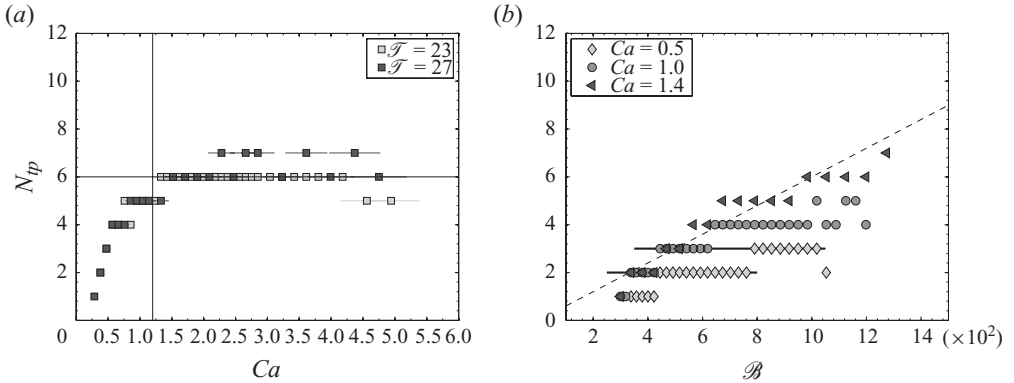


FIGURE 10. Number of turning points, N_{tp} , of the jet motion: (a) for several values of Ca and two values of \mathcal{T} , namely $\mathcal{T} = 23$ and 27 ; (b) for several values of \mathcal{B} and three values of Ca .

arrives at

$$h \sim r_j Ca^{-1} \mathcal{B}^{3/2}. \quad (5.6)$$

Observe that the dimensionless ratio $Ca^{-1} \mathcal{B}^{3/2}$ appears in expression (5.6) for the stable part of the jet and in expression (5.1) for the electrified-cone radius. It confirms the relevance of this dimensionless ratio in the axial evolution of the jet in the *steady region*.

6. Unsteady region: characterization of the whipping mode

This section is devoted to the experimental analysis of the whipping jet. Because the path of the jet motion may be unstable in time or in space, we firstly investigated the parametric range for which the path of the jet motion is or is not periodic. The digitalization of the jet path allows the number of loops of the jet to be clearly determined. This may be done by measuring the number of turning points in a digitalized jet path. The number of turning points, N_{tp} , of a jet as a function of either the capillary or the electrical Bond number is plotted in figure 10(a,b), respectively. Observe that the jet completes a loop every two turning points, although sometimes, it may break up into drops before completing a loop; see for example figure 1(b) where there is a jet path with three turning points but only one complete loop.

As shown in figure 10(a), the number of loops of the jet strongly depends on the value of the capillary number Ca . Results show that the number of loops increases with Ca within the range $Ca = 0.25$ – 1.2 and reaches a value practically constant, $N_{tp} = 6 \pm 1$ for $Ca > 4$, due to the unsteady nature of the point in which the jet breaks up into droplets. On the other hand, the effect of \mathcal{B} on the number of jet loops is quite different, since the number of loops remained practically constant for each experimental set, except for that of $Ca = 1.4$ (see figure 10b). Note that for $Ca = 1.4$, the number of turning points seems to linearly increase with the electrical Bond number to finally reach the value $N_{tp} = 6 \pm 1$. Thus, for capillary numbers smaller than 1.4, the influence of the electrical Bond number on the number of turning points of the jet path is rather limited compared with that of Ca . Increasing the capillary number makes the jet more unstable, and the number of loops increase.

Figure 11 shows the superposition of two digital pictures of a jet taken at two times separated by an interval of time Δt equal to one period. In each picture, the

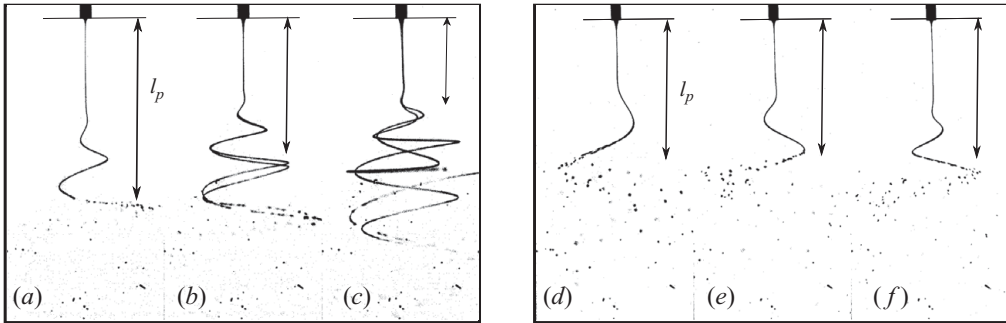


FIGURE 11. Overlapped images separated by one period of the jet detection ($\mathcal{T} = 23$): (a–c) $\mathcal{B} = 920$ and $Ca =$ (a) 0.6, (b) 1.5 and (c) 2.8; (d–f) $Ca = 0.5$ and $\mathcal{B} =$ (a) 340, (b) 540 and (c) 820.

part of the jet for which the jet motion is periodic and reproducible is defined by the axial distance l_p that is marked by an arrow. In the case of constant electrical Bond number, l_p decreases when the capillary number increases (see figure 11a–c). The jet path is spatially and temporally reproducible when the capillary number is kept constant (figure 11d–f) so that l_p remains the same independent of the value of the electrical Bond number; therefore, the images of the jet captured at times separated by multiples of one period are identical. In conclusion, the periodicity of the jet strongly depends on the capillary number, but it remains independent of the electrical Bond number. Experimental results showed the existence of three different regimes of jet motion as a function of the capillary number: periodic, quasi-periodic and chaotic. The different regimes of the whipping jet are identified as follows.

(a) At small values of the capillary number, $0.3 \leq Ca \lesssim 1.0$, the jet trajectories are periodic and perfectly reproducible, and the *periodic* length l_p is equal to the total length of the jet trajectory. Note that, in this regime, the liquid velocity Q/a^2 is lower than the velocity scale V_o and larger than the minimum velocity $Ca_{min} V_o$, for which the whipping exists.

(b) In the range of capillary numbers $1.0 \lesssim Ca \lesssim 2.8$, the whipping jet trajectories become chaotic after one or two wavelengths. In this quasi-periodic regime, only the first wavelengths of the jet trajectories are periodic and reproducible (see figure 11b). The ratio between the periodic length and the total length of the jet is smaller than 1 and decreases as a $-1/3$ power law of the capillary number. For values greater than $Ca \approx 1$, the liquid velocity is larger than the scale velocity V_o . As shown in the following, V_o is of the order of the phase velocity of the whipping jet so that the jet trajectories become quasi-periodic when the fluid velocity is greater than the phase velocity of the perturbation.

(c) For values of $Ca \gtrsim 2.8$, the trajectories of the whipping jet have the same behaviour as in the quasi-periodic regime, but the frequency, the wavelength of the whipping instability and the envelope of the jet trajectories are quite different (as shown in the following). Because the periodic length of the jet trajectory decreases with Ca , the trajectories of the whipping jet become chaotic before completing a full wavelength, and the whole jet is practically in a chaotic regime. Note that probably the jet remains periodic with an ordered behaviour when the number of loops remains low, but it becomes chaotic when it reaches a critical number of loops.

Concerning the wavelength of the whipping perturbation, in figure 12, several digital images of two jet trajectories separated by a time equal to a half-period are

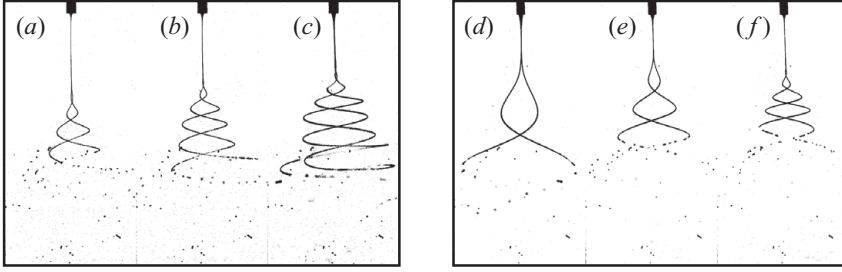


FIGURE 12. Digital images of two jet trajectories taken at times differing by a half-period $\Delta t/2$ ($\mathcal{T} = 23$): (a–c) $\mathcal{B} = 920$ and $Ca =$ (a) 0.6, (b) 1.0 and (c) 2.7; (d–f) $Ca = 1.0$ and $\mathcal{B} =$ (a) 320, (b) 490 and (c) 820.

presented. As shown in figure 12(a–c), the wavelength remained almost independent of the capillary number, whereas the electrical Bond number had a strong effect on the whipping wavelength (figure 12d–f). To confirm these observations, the dimensionless whipping wavelength λ/a is plotted in figure 13(a,b), the dimensionless whipping frequency $f a/V_o$ in figure 13(c,d) and the whipping phase velocity $f \lambda/V_o$ in figure 13(e,f) as a function of either the capillary number (figure 13a,c,e) or the electrical Bond number (figure 13b,d,f).

As a function of the capillary number, we found that the wavelength λ depends on the dimensionless time ratio \mathcal{T} , and it can be expressed as $\lambda \sim \lambda_o (\mathcal{T}/\mathcal{T}_o)$ with $\lambda_o = 12a = 1.4$ mm (figure 13a), while the frequency can be expressed as $f \sim f_o (\mathcal{T}/\mathcal{T}_o)^{-1}$ with $f_o = V_o/3a = 63$ Hz (figure 13c); f_o and λ_o are marked by the dashed lines, and the two solid lines mark an interval of $\pm 15\%$ around these values. Within the range of $0.3 \leq Ca \leq 2.8$, the dimensionless ratios $(\lambda/a)(\mathcal{T}_o/\mathcal{T})$ and $(f a/V_o)(\mathcal{T}/\mathcal{T}_o)$ have a constant value. For comparison, the value of the frequency reported by Shin *et al.* (2001) in their experiments with a PEO–water mixture in air has also been plotted and is represented with the white circles in figure 13(c). In their experiment, the authors fed a constant volumetric flow rate $Q = 0.2$ ml min $^{-1}$ of a PEO–water mixture through a stainless steel capillary tube of inner diameter 1 mm. The electric field in their experimental set-up was $E = 1.11$ kV cm $^{-1}$ over a distance of the order of 10^{-2} m. These experimental parameters correspond to $Ca = 0.4$, $\mathcal{T} = 2.4 \times 10^5$ and $\mathcal{B} \sim O(10^1 - 10^2)$. Resorting to long exposure times, the authors experimentally recorded the whipping envelope of this couple of fluids and fitted the experimental envelope by using an exponential law for the whipping amplitude of the type $A(z)/A_o \sim \exp[f z/U_o]$, U_o and $f = 0.014 \pm 0.002$ s $^{-1}$ being respectively the average fluid velocity at the capillary end and the frequency. Note that the experimental frequency reported by Shin *et al.* (2001) is in good agreement with ours results so that the expression $f_o (\mathcal{T}/\mathcal{T}_o)^{-1}$ may be used with confidence for the PEO–water mixture in spite of the very large difference in the electrical conductivity of the PEO–water mixture and the glycerine. Note, finally, that for $Ca > 2.8$, which corresponds to the chaotic regime, the wavelength and the frequency of the whipping slightly increase and decrease, respectively, with the capillary number. In consequence, as shown in figure 13(e), whatever the capillary number, the phase velocity of the whipping jet defined as the product of the dimensionless wavelength with the frequency is constant and equal to $f_o \lambda_o = 4V_o$ with an error of $\pm 15\%$ as shown by the two horizontal lines in the figure.

The wavelength and frequency of the whipping jet strongly vary with the electrical Bond number and follow power laws of the type $\mathcal{B}^{3/2}$ and $\mathcal{B}^{-3/2}$ respectively

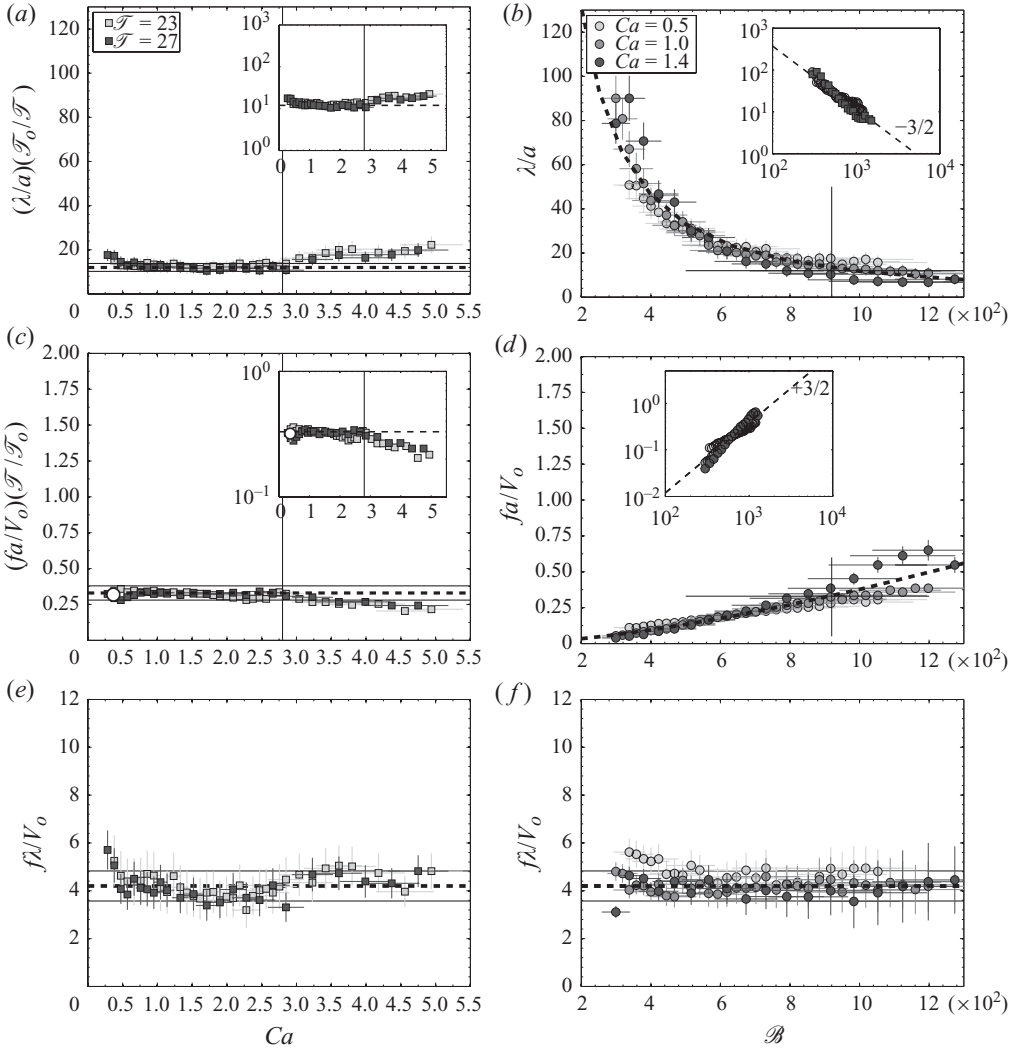


FIGURE 13. (a, b) Wavelength λ , (c, d) frequency f and (e, f) phase velocity $f\lambda$ of the whipping jet as a function of either (a, c, e) the capillary number at two fixed \mathcal{T} or (b, d, f) the electrical Bond number at three constant capillary number. In (a, c, e), $\mathcal{B} = 920$ and $\mathcal{T}_o = 23$; in (b, d, f), $\mathcal{T} = 23$. The white circles in (c) correspond to the results reported by Shin *et al.* (2001).

(figure 13b,d). Note that the whipping phase velocity $f\lambda$ is practically independent of the electrical Bond number within the error band of $\pm 15\%$ (figure 13f).

In conclusion, the phase velocity of the jet whipping depends only on the visco-capillary scale velocity V_o , and its value is equal to $f_o\lambda_o = 4V_o = 8.8\text{ cm s}^{-1}$ for the glycerine–hexane pair. The wavelength λ and the frequency f of the jet whipping can be expressed as

$$\lambda = \lambda_o (\mathcal{B}/\mathcal{B}_o)^{-3/2} (\mathcal{T}/\mathcal{T}_o), \quad f = f_o (\mathcal{B}/\mathcal{B}_o)^{3/2} (\mathcal{T}/\mathcal{T}_o)^{-1}, \quad (6.1)$$

with $\mathcal{B}_o = 920$, $\mathcal{T}_o = 23$, $\lambda_o = 12a$ and $f_o = V_o/3a$.

These results confirm the destabilizing effect of the electrical field on the jet trajectory as it has been typically observed in electro-spinning experiments (Hohman

et al. 2001*b*; Shin *et al.* 2001) or in the experiments carried out by Taylor (1969). In fact, an increase in the applied voltage increases both the electrical field and the charge density of the jet (see (5.5)). The jet becomes more unstable, increasing its whipping frequency, as was commented by Hohman *et al.* (2001*b*), and reducing its characteristic wavelength.

Now, the behaviour of the whipping envelope is analysed as a function of the dimensionless parameters Ca and \mathcal{B} . Figure 9 shows some examples of the whipping envelope for different values of the dimensionless parameters. The evolution of the whipping envelope is plotted as a function of the capillary number in figure 14(*a,c,e*) and as that of the electrical Bond number in figure 14(*b,d,f*). The amplitude A and the axial distance z are normalized with the needle radius a . As shown in figure 14(*a*), two regimes may be identified: for $Ca \leq 2.8$, which corresponds to the periodic and quasi-periodic regimes, the amplitude A and length h_w of the envelope increase with the capillary number, while the envelope remains unchanged for $Ca > 2.8$. This value of the capillary number corresponds to the transition from the quasi-periodic to the chaotic regime of the jet path. Note that the downstream behaviour of the envelope also changes with the capillary number until the envelope reaches an asymptotic universal shape at $Ca = 2.8$. Thus, for a capillary number larger than 2.8, the frequency, the wavelength and the envelope of the jet exhibit a different behaviour from that in the periodic and quasi-periodic regimes. The shape of the different envelopes has been compared with that obtained by Shin *et al.* (2001) using a PEO–water mixture in air; the amplitude of the latter envelope is represented by the meridional line of white crosses in figure 14(*a*). Remember that the dimensionless parameters of their experiment were $Ca = 0.4$, $\mathcal{T} = 2.4 \times 10^5$ and $\mathcal{B} \sim O(10^1-10^2)$, which are higher than the minimum dimensionless values Ca_{min} , \mathcal{T}_{min} and \mathcal{B}_{min} for which the whipping instability develops in the case of the glycerine–hexane fluid couple. The envelope obtained by Shin *et al.* (2001) presents a different downstream behaviour from the glycerine–hexane case.

In the former case, the jet begins to bend at a smaller distance from the capillary so that the envelope amplitude is larger near the needle than in the latter case; also, in their case, the amplitude of the envelope of the whipping jet is two times larger than in ours. It is only for larger capillary numbers, $Ca > 2$, or far from the needle, $z > 40a$, that the envelope amplitude of the glycerine jet reaches the envelope amplitude of the PEO–water mixture. Let us finally remark that the differences between the case reported by Shin *et al.* (2001) and ours lie in the fact that, firstly, the PEO–water mixture is a non-Newtonian fluid and, secondly, the dimensionless time ratio \mathcal{T} was 10^4 times larger in the case of Shin *et al.* (2001) than in ours. Finally, the difference in the geometry of the electrical configuration (a plate–plate geometric configuration in theirs and a capillary–plate configuration in ours) may also play a role in the envelope behaviour.

For ultra-fine polymer fibres, Fridrikh *et al.* (2003, 2006) proposed a slender-body model and the following analysis to explain the behaviour of the jet amplitude. In the early stages of whipping, the amplitude of the whipping instability grows exponentially with time and is controlled by charge repulsion and inertia. In the later stages, the envelope of the whipping jet is controlled by charge repulsion and stretching viscosity. At the end, whipping is controlled by the balance between surface charge repulsion (destabilizing effect) and surface tension (stabilizing effect), which leads to the jet radius relation $r_j \sim (Q/I)^{2/3}$. Unfortunately, the model proposed by Fridrikh *et al.* (2006) leads to a whipping amplitude much larger than the experimental amplitude observed for a polymer jet in air. On the other hand, the Lagrangian model proposed

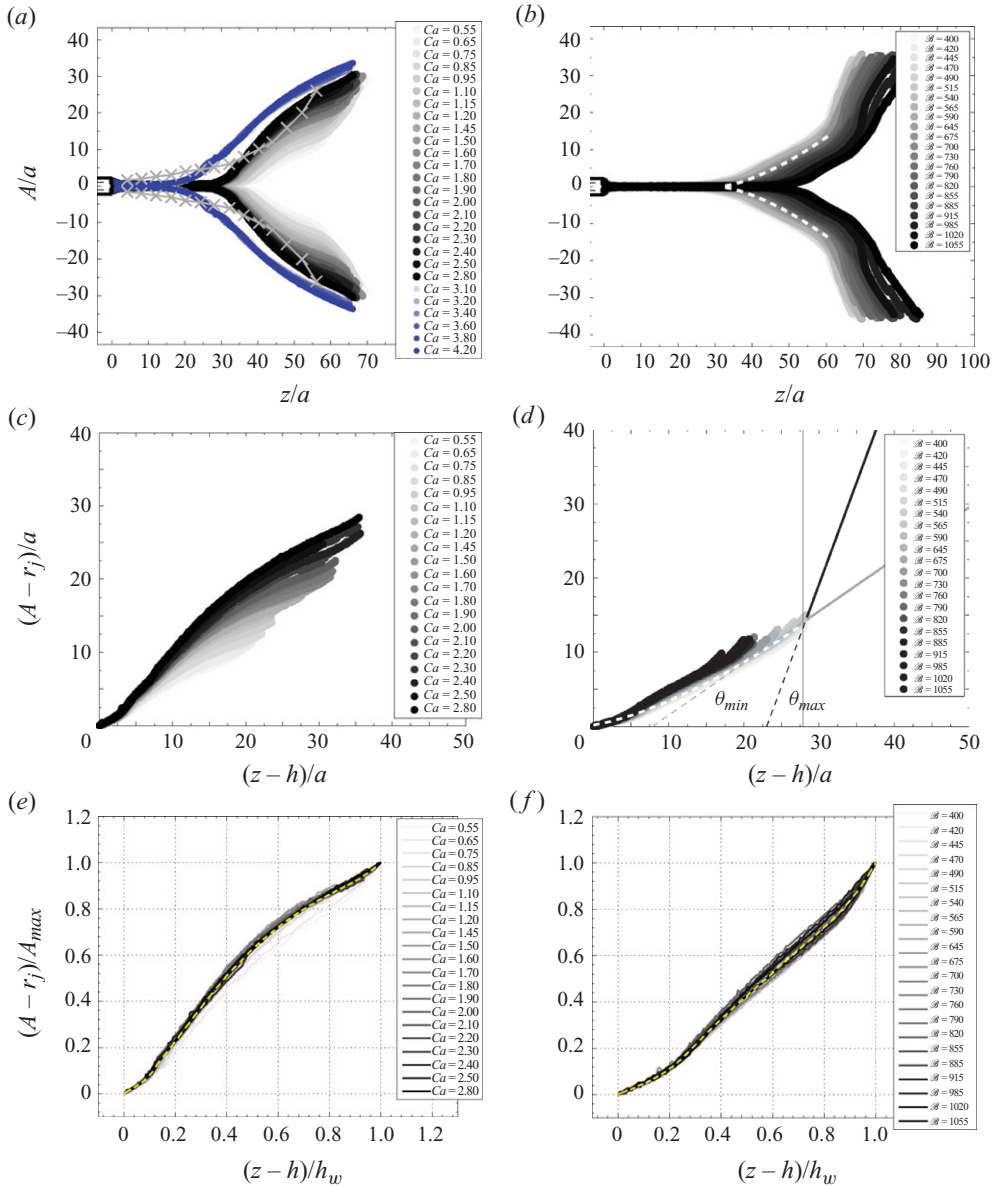


FIGURE 14. (Colour online) Amplitude of the envelope versus the axial distance as a function of either (a, c, e) the capillary number or (b, d, e) the electrical Bond number. (a, b) Digital meridional images of the whipping envelope. (c, d) Meridional curves of the whipping envelope without the steady region or the droplet region. (e, f) Normalized whipping envelope.

by Reneker and coworkers (Reneker *et al.* 2000; Yarin *et al.* 2001), which takes into account the surface tension, electrical and viscoelastic forces, permits the reproduction of the bending motion of the jet. The balance between surface tension and electrical and viscoelastic forces acting on a jet seems to be the principal forces controlling the whipping motion of a non-Newtonian jet in air.

The shape of the whipping envelope depends on the electrical Bond number (figure 14b). Essentially, the length of the whipping envelope, h_w , decreases because

of the increase of the length h with the electrical Bond number; on the contrary, the maximum angle of the droplet trajectories remains almost independent of \mathcal{B} . For comparison, we have also plotted a meridional curve of an envelope (white dashed line in figure 14*b*), which has been obtained empirically in the case of $\mathcal{B} = 540$ (see (6.2)); the agreement with the experimental envelope is quite good.

For a better comparison of the different experimental envelope curves, it proves convenient to plot the dimensionless quantity $(A - r_j)/a$ versus $(z - h)/a$. As shown in figure 14*c*), both the amplitude of the envelope and the length of the whipping increase with the capillary number. We have noted that the amplitude of the envelope and the length of the whipping follow respectively the 2/3 and 1/3 power laws of the capillary number. The increase of h_w was expected, since the diameter of the jet is essentially controlled by the capillary number, and thicker jets will take longer to disintegrate. Also, the amplitude of the whipping instability increases with Ca , since the Coulomb repulsion at the whipping and charged droplet zones also increases with the capillary number. On the other hand, the whipping envelopes are independent of the electrical Bond number; therefore, the meridional curves of the envelope obtained at different values of \mathcal{B} overlap. Thus, the dependence on the electrical Bond number of both the length and the maximum amplitude of the whipping envelope are rather small compared with their dependence on the capillary number. Note that contrary to the behaviour of the shape of the envelope, the length h of the stable part of the jet depends on the electrical Bond number (figure 8*a*). Observe also that the maximum angle θ that forms the droplet trajectories with the jet axis depends on the capillary number, but it is independent of the electrical Bond number. For all combinations of values of the capillary and electrical Bond numbers studied, the maximum angle of droplet trajectories was within the range $\theta_{min} = 35^\circ$ and $\theta_{max} = 70^\circ$. The two extrema angles are plotted in figure 14*d*).

Since the shapes of the whipping envelopes seem very similar to each other, we have normalized them with the maximum amplitude A_{max} , while the abscissa $z-h$ has also been normalized using the whipping length h_w . Results, which are plotted in figure 14*e,f*), confirm the collapse of the whipping envelopes onto a single curve. Nonetheless, one should be aware that this self-similar behaviour is observed only in the periodic and quasi-periodic regimes of the jet trajectories. Self-similar behaviour of the envelopes has been also observed in experiments carried out at two other values of the capillary number, $Ca = 1.0$ and 1.4 , as a function of the electrical Bond number. We have calculated the mean curve of the normalized amplitude of the envelopes for each case: an example of the mean curves is represented by the dashed lines in figure 14*e,f*); the two cases correspond respectively to the mean curve for a given electrical Bond number and several values of the capillary number (figure 14*e*) and the mean curve for a given capillary number and several values of the electrical Bond number (figure 14*f*). The mean curves permit the comparison of the normalized amplitude of the envelopes for different values of Ca and \mathcal{B} .

In figure 15*a*), we have plotted for comparison the different mean curves of the envelopes on log-log axes. In the range of $(z - h)/h_w$ between 10^{-2} and 10^{-1} , the mean envelope behaves linearly with the normalized axial distance and closely follows a law of the type $[(z - h)/h_w]$ for different electrical Bond and capillary numbers. Observe that this region $(z - h)/h_w = O[10^{-2}-10^{-1}]$ is very small compared with the total length scale of the envelope; it is approximately of the order of 10 % of the total envelope length. Within the range of the abscissa $0.1 \leq (z - h)/h_w \leq 0.4$, which corresponds to 30 % of the total envelope length, the different curves collapse onto just one universal curve that follows a power law of the type $[(z - h)/h_w]^{3/2}$ with

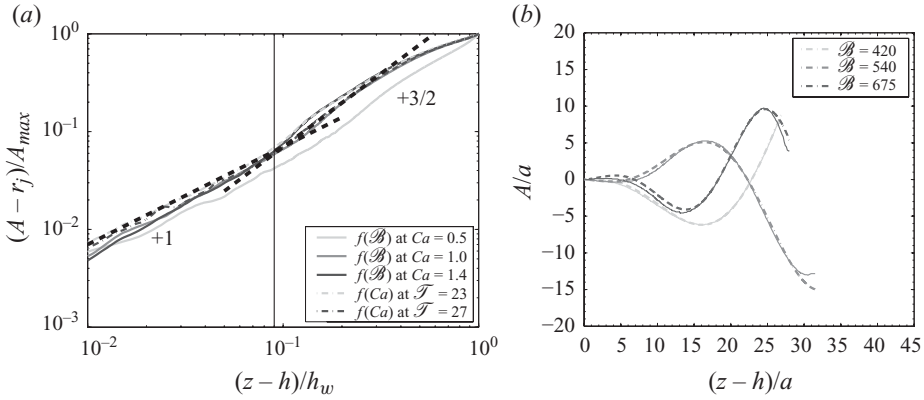


FIGURE 15. (a) Comparison of the normalized mean curves of the whipping envelopes from different experiments. (b) Comparison of the whipping jet images (straight line) and the corresponding theoretical formula (dashed line) for different values of the electrical Bond number ($Ca = 0.5$, $\mathcal{F} = 23$).

the capillary and the electrical Bond numbers within the studied range, $Ca \approx 0.5\text{--}2.8$ and $\mathcal{B} \approx 400\text{--}1055$. Let us finally remark that this result is quite different from the experimental observation reported by Shin *et al.* (2001) for an electrified jet of a mixture of PEO and water, for which they found a normalized whipping amplitude $A(z)/A_0$ following the exponential law $\exp[\omega z/U_0]$.

Using properly the experimental results, we modelled the amplitude of the whipping oscillation as

$$A(z, t) = L \left(\frac{z - h}{c} \right)^\alpha \cos \left[\left(\frac{2\pi(z - h)}{\lambda} \right)^\xi + 2\pi f t + \varphi \right], \quad (6.2)$$

where the exponents $\alpha = 3/2$ and $\xi \approx 1$ take into account the downstream evolution of the wavelength; c and L are characteristic lengths and φ is a phase amplitude. The mean values of c and L were 0.19 and 0.78 mm, respectively. It should be noted that expression (6.2) may be applied only within the zone of completely periodical whipping jet trajectories, e.g. for $z < l_p$. A comparison between several examples of the whipping jet images and the corresponding empirical formula are plotted in figure 15(b). The curve was obtained empirically and the experimental curves match quite well. Of course, the envelope obtained by overlapping the empirical curves at different times throughout one period ($1/f$) is also in good agreement with the experimental whipping envelopes (white dashed line in figure 14b,d). These results show that expression (6.2) is pertinent to model the whipping instability in the periodic and quasi-periodic regimes.

7. Conclusion

The research described in this paper has been carried out to experimentally characterize the whipping motion of an electrified micro-jet of glycerine immersed within a liquid bath. In particular, the evolution of the frequency f , the wavelength λ and the amplitude A of the whipping oscillations as a function of the governing parameters of the experiment, namely the applied electrical voltage and the flow rate, has been determined. Experimental results have shown that the whipping motion might be characterized by three dimensionless parameters: the capillary number Ca ,

the electrical Bond number \mathcal{B} and, finally, the ratio between the residence time and the electrical relaxation time, \mathcal{T} . The presence of whipping requires threshold values of the three parameters (Ca_{min} , \mathcal{B}_{min} , \mathcal{T}_{min}) to be reached or equivalently requires that the liquid velocity reaches a value expressed by (5.4). The electrical current transported through the jet followed a radically different behaviour from that given in earlier papers on electro-sprays. Contrary to electro-spray experiments, in this configuration both convection and conduction transports are important. The elongation and the radius of the electrified cone strongly depend on the capillary and electrical Bond numbers. On the other hand, the radius of the electrified jet seems to be independent of the downstream distance and varied as $Ca^{3/4} \mathcal{B}^{-1/2}$. The charge density decreases with the capillary number, while it increases with both \mathcal{T} and \mathcal{B} and can be expressed as a function of the reduced velocity v/V_o . In consequence, the normal electric field at the jet surface decreases (increases) with Ca (\mathcal{B} and \mathcal{T}) so that an infinitely long jet becomes more stable when Ca increases or either \mathcal{B} or \mathcal{T} decrease. Contrary to the expected for very long jets, the axial downstream distance h measured from the capillary exit, which defines the starting point at which the jet bends, increases, that is, the jet becomes more stable, when either Ca decreases or \mathcal{B} increases. This unexpected behaviour is a consequence of Coulomb repulsion of the space charge onto the moving jet and the droplets. The whipping behaviour, which depends strongly on the capillary number but only weakly on the electrical Bond number, presents three different regimes: periodic, quasi-periodic or chaotic. Results have shown that the wavelength λ and the frequency f of the jet whipping depend strongly on the electrical Bond number and can be expressed with (6.2). Whatever the capillary and the electrical Bond number, the phase velocity of the whipping jet, $f\lambda = 4V_o$, is constant and depends only on the visco-capillary scale velocity V_o , confirming the scaling of the problem. The detected whipping envelope showed self-similar behaviour after appropriate normalization. The amplitudes of the different mean whipping envelopes normalized with the maximum amplitude evolved downstream towards a sole curve showing a 3/2 power law of the normalized distance.

The obtained results illustrate clearly the general behaviour of these lateral instabilities and can be useful to understand the complex underlying dynamics. The experimental observations and results provided in this work lead the way for future work. Future numerical or theoretical work must take into account the conduction charge transport by the whipping jet. Experiments with other couples of liquids should be carried out to confirm the different experimental relations, in particular the dependence of the electrical current, jet radius and whipping jet behaviour as a function of the dimensionless parameters.

We wish to dedicate this work to the memory of our friend, colleague and co-author of this paper, Professor A. Barrero, who passed away on 25 April while this manuscript was being refereed. Without his deep physical insight and continuous encouragement to all of us until the end of his days, neither this paper nor many other things would have been possible. This research has been conducted under the partial support of the Ministry of Science and Innovation (Projects DPI 2007-66659-C03-01 and DPI 2007-66659-C03-03). Support by a grant from Yflow SL is gratefully acknowledged. The authors thank S. Magnabal, student at the ENSEEIHT, Toulouse, for his valuable assistance during his internship at the Escuela Técnica Superior de Ingenieros of the Universidad de Sevilla. The authors are also indebted to Professor A. Fernández-Nieves from Georgia Tech for his valuable comments.

Appendix. Relative importance of the outer flow on the jet dynamics

The hexane is set in motion by the glycerine jet flowing through it. The thickness δ_e of the hexane viscous layer, which surrounds the glycerine jet and grows downstream, is proportional to the square root of the kinematic viscosity of the hexane multiplied by the convective time, $\delta_e \sim \sqrt{\nu_e h/v}$, where $v = Q/(\pi r_j^2)$ is the velocity of the liquid in the jet. Therefore, the order of magnitude of the tangential viscous stress acting on the jet interface is $\tau = \mu_e (\partial v / \partial n) \sim \mu_e (v / \delta_e)$, n being the outer normal to the jet interface. The resistance that the boundary layer of hexane exerts on the glycerine jet will be negligible as long as the viscous stress τ is much smaller than the tangential electrical stress, $\tau \ll \epsilon_e E_n E_t$, which implies that

$$\left(\frac{\mu_e^2 v^3}{\nu_e h} \right)^{1/2} \ll \frac{\gamma}{r_j} \frac{h}{r_j}, \quad (\text{A } 1)$$

where, we have used the relations $\epsilon_e E_n^2 \sim \gamma / r_j$ and $E_n / E_t \sim r_j / h$. Introducing $Q = v r_j^2$ and (5.2) and (5.6), expression (A 1) reads

$$\left(\frac{\mu_e}{\mu} \mathcal{S} \right)^{1/2} Ca^{-11/8} \mathcal{B}^{-1} \ll 1, \quad (\text{A } 2)$$

which clearly shows that the influence of the outer bath on the jet dynamic may be neglected for the values of Ca and \mathcal{B} used in the experiment ($\mathcal{S} = 1.3 \times 10^{-3}$ and $(\mu_e / \mu) = 2.3 \times 10^{-4}$). In the case of an electrified jet of glycerine, it is worth noting that the principal advantage of using a liquid bath instead of air is the halving of the surface tension coefficient between the two fluids. Because the surface tension appears in all the dimensionless numbers of the problem, the use of a hexane bath allows the minimum values of the capillary and electrical Bond numbers and the dimensionless time, for which the whipping instability grows and develops, to be reached.

REFERENCES

- BARRERO, A., LÓPEZ-HERRERA, J. M., BOUCARD, A., LOSCERTALES, I. G. & MÁRQUEZ, M. 2004 Steady cone-jet electrosprays in liquid insulator baths. *J. Colloid Interface Sci.* **272**, 104–108.
- BARRERO, A. & LOSCERTALES, I. G. 2007 Micro- and nanoparticles via capillary flows. *Annu. Rev. Fluid Mech.* **39**, 89–106.
- BASSETT, E. B. 1894 Waves and jets in a viscous liquid. *Am. J. Math.* **16**, 93–110.
- BOURRIÈRES, F. J. 1939 *Sur un Phénomène d'Oscillation Auto-Entretenu en Mécanique des Fluides Réels*, Publications Scientifiques et Techniques du Ministère de l'Air, vol. 147. Gauthier-Villars
- CLOUPEAU, M. & PRUNET-FOCH, B. 1989 Electrostatic spraying of liquids in cone-jet mode. *J. Electrostat.* **22**, 135–159.
- DÍAZ, J. E., BARRERO, A., MÁRQUEZ, M. & LOSCERTALES, I. G. 2006 Controlled encapsulation of hydrophobic liquids in hydrophilic polymer nanofibers by co-electrospinning hydrophilic polymer nanofibers by co-electrospinning. *Adv. Funct. Mater.* **16**, 2110–2116.
- DOARÉ, O. & DE LANGRE, E. 2002 The flow-induced instability of long hanging pipes. *Eur. J. Mech. A* **21**, 857–867.
- DOSHI, J. & RENEKER, D. H. 1995 Electrospinning process and applications of electrospun fibers. *J. Electrostat.* **35** (2–3), 151–160.
- FERNÁNDEZ DE LA MORA, J. & LOSCERTALES, I. G. 1994 The current emitted by highly conducting Taylor cones. *J. Fluid Mech.* **260**, 155–184.
- FRIDRIKH, S. V., YU, J. H., BRENNER, M. P. & RUTLEDGE, G. C. 2003 Controlling the fiber diameter during electrospinning. *Phys. Rev. Lett.* **90** (14), 144502.

- FRIDRIKH, S. V., YU, J. H., BRENNER, M. P. & RUTLEDGE, G. C. 2006 Nonlinear whipping behaviour of electrified fluid jets. In *Polymeric Nanofibers* (ed. D. H. Reneker & H. Fong), American Chemical Society Symposium Series, vol. 918, pp. 36–55. American Chemical Society.
- GAÑÁN-CALVO, A. M., DÁVILA, J. & BARRERO, A. 1997 Current and droplet size in the electrospaying of liquids: scaling laws. *J. Aerosol Sci.* **28** (2), 249–275.
- HARTMAN, R. P. A., BRUNNER, D. J., CAMELOT, D. M. A., MARIJNISSEN, J. C. M. & SCARLETT, B. 2000 Jet break-up in electrohydrodynamic atomization in the cone-jet mode. *J. Aerosol Sci.* **31** (1), 65–95.
- HIGUERA, F. J. 2006 Stationary viscosity-dominated electrified capillary jets. *J. Fluid Mech.* **558**, 143–152.
- HIGUERA, F. J. 2010 Numerical computation of the domain of operation of an electro spray of a very viscous liquid. *J. Fluid Mech.* **648**, 35–52.
- HOHMAN, M. M., SHIN, M., RUTLEDGE, G. & BRENNER, M. P. 2001a Electrospinning and electrically forced jets. Part I. Stability theory. *Phys. Fluids* **13** (8), 2201–2220.
- HOHMAN, M. M., SHIN, M., RUTLEDGE, G. & BRENNER, M. P. 2001b Electrospinning and electrically forced jets. Part II. Applications. *Phys. Fluids* **13** (8), 2221–2236.
- JAEGER, R., BERGSHOFF, M. M., BATTLE, C. M., SCHÖNHER, H. & VANSO, G. J. 1998 Electrospinning of ultrathin polymer fibers. *Macromol. Symp.* **127**, 141–150.
- LALLAVE, M., BEDIA, J., RUIZ-ROSAS, R., RODRÍGUEZ-MIRASOL, J., CORDERO, T., OTERO, J. C., MARQUEZ, M., BARRERO, A. & LOSCERTALES, I. G. 2007 Filled and hollow carbon nanofibers by coaxial electrospinning of Alcell lignin without binder polymers. *Adv. Mater.* **19**, 4292–4296.
- DE LANGRE, E., PAÏDOUSSIS, M. P., DOARÉ, OLIVIER & MODARRES-SADEGHI, Y. 2007 Flutter of long flexible cylinders in axial flow. *J. Fluid Mech.* **571**, 371–389.
- LARSEN, G., VELARDE-ORTIZ, R., MINCHOW, K., BARRERO, A. & LOSCERTALES, I. G. 2003 A method for making inorganic and hybrid (organic/inorganic) fibers and vesicles with diameters in the submicrometer and micrometer range via sol-gel chemistry and electrically forced liquid jets. *J. Am. Chem. Soc.* **125**, 1154–1155.
- LEMAITRE, C., HÉMON, P. & DE LANGRE, E. 2005 Instability of a long ribbon hanging in axial air flow. *J. Fluid Struct.* **20**, 913–925.
- LI, D. & XIA, Y. 2004 Direct fabrication of composite and ceramic hollow nanofibers by electrospinning. *Nano Lett.* **4** (5), 933–938.
- LI, F., YIN, X.-Y. & YIN, X.-Z. 2008 Instability of a viscous coflowing jet in a radial electric field. *J. Fluid Mech.* **596**, 285–311.
- LI, F., YIN, X.-Y. & YIN, X.-Z. 2009 Axisymmetric and non-axisymmetric instability of an electrified viscous coaxial jet. *J. Fluid Mech.* **632**, 199–225.
- LISTER, J. R. & STONE, H. A. 1998 Capillary breakup of a viscous thread surrounded by another viscous fluid. *Phys. Fluids* **10** (11), 2758–2765.
- LÓPEZ-HERRERA, J. M., BARRERO, A., LÓPEZ, A., LOSCERTALES, I. G. & MÁRQUEZ, M. 2003 Coaxial jets generated from electrified Taylor cones. scaling laws. *J. Aerosol Sci.* **34** (5), 535–552.
- LOSCERTALES, I. G., BARRERO, A., GUERRERO, I., CORTIJO, R., MÁRQUEZ, M. & GAÑÁN-CALVO, A. M. 2002 Micro/nano encapsulation via electrified coaxial liquid jets. *Science* **295**, 1695–1698.
- LOSCERTALES, I. G., BARRERO, A., MÁRQUEZ, M., SPRETZ, R., VELARDE-ORTIZ, R. & LARSEN, G. 2004 Electrically forced coaxial nanojets for one-step hollow nanofiber design. *J. Am. Chem. Soc.* **126**, 5376–5377.
- MARÍN, A. G., LOSCERTALES, I. G., MÁRQUEZ, M. & BARRERO, A. 2007 Simple and double emulsions via coaxial jet electrospays. *Phys. Rev. Lett.* **98**, 014502.
- MESTEL, A. J. 1994 Electrohydrodynamic stability of a slightly viscous jet. *J. Fluid Mech. Digit. Arch.* **274** (1), 93–113.
- MESTEL, A. J. 1996 Electrohydrodynamic stability of a highly viscous jet. *J. Fluid Mech. Digit. Arch.* **312** (1), 311–326.
- PAÏDOUSSIS, M. P. 1998 *Fluid–Structure Interactions: Slender Structures and Axial Flow*, vol. 1. Academic.
- RENEKER, D. H. & YARIN, A. L. 2008 Electrospinning jets and polymer nanofibers. *Polymer* **49**, 2387–2425.
- RENEKER, D. H., YARIN, A. L., FONG, H. & KOOMBHONGSE, S. 2000 Bending instability of electrically charged liquid jets of polymer solutions in electrospinning. *J. Appl. Phys.* **87** (9), 4531–4547.

- RISTROPH, L. & ZHANG, J. 2008 Anomalous hydrodynamic drafting of interacting flapping flags. *Phys. Rev. Lett.* **101**, 194502/1–4.
- RUO, A.-C., CHEN, F. & CHANG, M.-H. 2009 Linear instability of compound jets with nonaxisymmetric disturbances. *Phys. Fluids* **21** (1), 012101.
- SHIN, Y. M., HOHMAN, M. M., BRENNER, M. P. & RUTLEDGE, G. C. 2001 Experimental characterization of electrospinning: the electrically forced jet and instabilities. *Polymer* **42**, 9955–9967.
- SUN, Z., ZUSSMAN, E., YARIN, A. L., WENDORFF, J. H. & GREINER, A. 2003 Compound core-shell polymer nanofibers. *Adv. Mat.* **15**, 1929–1936.
- TAYLOR, G. 1969 Electrically driven jets. *Proc. R. Soc. A* **313**, 453–475.
- THERON, S. A., ZUSSMAN, E. & YARIN, A. L. 2004 Experimental investigation of the governing parameters in the electrospinning of polymer solutions. *Polymer* **45**, 2017–2030.
- WILLIAMSON, C. H. K. & GOVARDHAN, R. 2004 Vortex-induced vibrations. *Annu. Rev. Fluid Mech.* **36**, 413–455.
- YARIN, A. L., KOOMBHONGSE, S. & RENEKER, D. H. 2001 Bending instability in electrospinning of nanofibers. *J. Appl. Phys.* **89**, 3018–3026.
- ZELENY, J. 1917 Instability of electrified liquid surfaces. *Phys. Rev.* **10** (1), 1–6.
- ZHANG, J., CHILDRESS, S., LIBCHABER, A. & SHELLEY, M. 2000 Flexible filaments in a flowing soap film as a model for one-dimensional flags in a two dimensional wind. *Nature* **408**, 835–839.
- ZHANG, X. & BASARAN, O. A. 1996 Dynamics of drop formation from a capillary in the presence of an electric field. *J. Fluid Mech.* **326**, 239–263.